

Tuning the carrier localization, magnetic and thermoelectric properties of ultrathin $(\text{LaNiO}_{3-\delta})_1/(\text{LaAlO}_3)_1(001)$ superlattices by oxygen vacancies

Manish Verma* and Rossitza Pentcheva†

Department of Physics and Center for Nanointegration (CENIDE), Universität Duisburg-Essen, Lotharstr. 1, 47057 Duisburg, Germany

 (Received 26 October 2022; revised 16 November 2023; accepted 4 December 2023; published 21 February 2024)

Using a combination of density functional theory calculations with an on-site Coulomb repulsion term (DFT+ U) and Boltzmann transport theory within the constant relaxation time approximation, we explore the effect of oxygen vacancies on the electronic, magnetic, and thermoelectric properties in ultrathin $(\text{LaNiO}_{3-\delta})_1/(\text{LaAlO}_3)_1(001)$ superlattices (SLs). For the pristine SL ($\delta = 0$), an antiferromagnetic charge-disproportionated (AFM-CD) $(d^8\bar{L}^2)_{S=0}(d^8)_{S=1}$ phase is stabilized, irrespective of strain. At $\delta = 0.125$ and 0.25 , the localization of electrons released from the oxygen defects in the NiO_2 plane triggers a charge-disproportionation, leading to a ferrimagnetic insulator both at a_{SrTiO_3} (tensile strain) and a_{LaSrAlO_4} (compressive strain). At $\delta = 0.5$, an insulating phase emerges with alternating stripes of Ni^{2+} (high-spin) and Ni^{2+} (low-spin) and oxygen vacancies ordered along the $[110]$ direction (S-AFM), irrespective of strain. This results in a robust n -type in-plane power factor of $24 \mu\text{W}/\text{K}^2 \text{ cm}$ at a_{STO} and $14 \mu\text{W}/\text{K}^2 \text{ cm}$ at a_{LSAO} at 300 K (assuming relaxation time $\tau = 4$ fs). Additionally, the pristine and $\delta = 0.5$ SLs are shown to be dynamically stable. This demonstrates the fine tunability of electronic, magnetic, and thermoelectric properties of ultrathin nickelate superlattices by oxygen vacancies.

DOI: [10.1103/PhysRevResearch.6.013189](https://doi.org/10.1103/PhysRevResearch.6.013189)

I. INTRODUCTION

Understanding the physics of strongly correlated electrons in transition metal oxides (TMO) in the ultrathin limit is at the forefront of condensed matter physics, as they are susceptible to collective ordering phenomena resulting in spin- and charge-ordered phases different from the bulk [1–5]. Engineering such phases became viable due to the possibility to grow such heterostructures with atomically sharp interfaces [4].

In the context of designing novel quantum phases, bulk LaNiO_3 —a paramagnetic metal down to the lowest temperature (T) [6]—represents a model system. In contrast, the other members of the rare-earth-nickelate series (RNiO_3 , $R = \text{Ce-Lu}$), by virtue of small or negative charge transfer energy [7–15], undergo a metal-to-insulator transition (MIT) due to charge-disproportionation (CD) [8,16–18]. This is further accompanied by a symmetry lowering from an orthorhombic ($Pbnm$) to a monoclinic ($P2_1/n$) structure at low T , and additionally by an onset of antiferromagnetic (AFM) order in the case of PrNiO_3 and NdNiO_3 [19]. In this picture, MIT stems from the volume collapse of half of the NiO_6 octahedra with two ligand holes around the central Ni ($d^8\bar{L}^2$) site, while the other octahedra expand accordingly with little effect on the net

volume of the unit cell, as observed experimentally [6]. This is viewed as $(d^8\bar{L})(d^8\bar{L}) \rightarrow (d^8\bar{L}^2)_{S=0}(d^8)_{S=1}$, where S is the total spin, spanning both Ni and O sites. Moreover, the $d^8\bar{L}^2$ configuration of the collapsed octahedra is equivalent to a $3d^6$ occupation that is low spin. Notably, in the case of charge-disproportionation or breathing-mode distortion, the two Ni sites $[(d^8\bar{L}^2)_{S=0}$ and $(d^8)_{S=1}]$ remain Jahn-Teller inactive, for instance, in LuNiO_3 [20].

In contrast to bulk, when LaNiO_3 is grown as an ultrathin superlattice (SL), it undergoes a MIT below a critical thickness of two monolayers (ML), triggered by the effect of confinement [21–31]. Apart from MIT, an antiferromagnetic charge-disproportionated (AFM-CD) phase was observed in $(\text{LaNiO}_3)_2/(\text{LaAlO}_3)_2(001)$ SLs upon cooling, irrespective of strain [32]. Furthermore, Middey *et al.* [33] also recently reported an AFM-CD phase leading to MIT in ultrathin RNiO_3 SLs. Previous DFT+ U studies [21–23] identified charge-disproportionation on the Ni sites with ferromagnetic coupling (FM-CD) as a possible mechanism behind the MIT in $(\text{LaNiO}_3)_1/(\text{LaAlO}_3)_1(001)$ (1/1) SL at the lateral lattice constant of SrTiO_3 (tensile strain), and a semi-metallic phase with less pronounced CD at compressive strain. On the other hand, Puggioni *et al.* [34] reported an AFM-CD phase in $(\text{LaNiO}_3)_1/(\text{LaAlO}_3)_1(001)$ SL using a laterally elongated supercell and the variational self-interaction-corrected local density functional theory [35,36], irrespective of strain. They argued that the DFT+ U approach is insufficient to describe their findings. Hence the question arises whether DFT+ U can explain the AFM-CD insulating phase in $(\text{LaNiO}_3)_1/(\text{LaAlO}_3)_1(001)$ SL.

Apart from LaNiO_3 bulk and superlattices, there is a recent interest in understanding the electronic and magnetic properties of oxygen-deficient $\text{LaNiO}_{3-\delta}$ bulk [37–41] and

*manish.verma@uni-due.de

†rossitza.pentcheva@uni-due.de

Published by the American Physical Society under the terms of the [Creative Commons Attribution 4.0 International](https://creativecommons.org/licenses/by/4.0/) license. Further distribution of this work must maintain attribution to the author(s) and the published article's title, journal citation, and DOI.

thin films [42,43]. Oxygen vacancies are also present in other bulk $R\text{NiO}_3$. Recently, Kotiuga *et al.* [44,45] reported that the electrons released by oxygen vacancies in bulk SmNiO_3 and NdNiO_3 were localized at the Ni sites, opening a Mott insulating gap, stemming from the interplay of crystal field splitting (CFS) and strongly correlated electrons in the Ni $3d$ orbitals. Using DFT+ U , Shin *et al.* explored the electronic and magnetic structure of bulk $\text{LaNiO}_{3-\delta}$ ($\delta = 0.25$ and 0.5) with ordered oxygen vacancies [46]. Although oxygen vacancies create localized defect states below the Fermi level in bulk LaNiO_3 , a gap is not formed, at least at low oxygen vacancy concentrations [47].

Oxygen defects are ubiquitous also in ultrathin $\text{LaNiO}_3/\text{LaAlO}_3(001)$ SLs, either under tensile strain [32] or due to the polar interface to the SrTiO_3 substrate [48]. Hence it is important to clarify, how oxygen vacancies influence the electronic and magnetic properties of a $(\text{LaNiO}_3)_1/(\text{LaAlO}_3)_1(001)$ SL and whether they can cause a charge localization induced gap opening under confinement and strain. While a recent DFT+ U study investigated the electronic and magnetic properties of the oxygen deficient $(\text{LaNiO}_3)_1/(\text{LaAlO}_3)_1(001)$ SLs, at low oxygen vacancy concentrations [49], here we concentrate on $(\text{LaNiO}_{3-\delta})_1/(\text{LaAlO}_3)_1(001)$ SLs with $\delta = 0.125 - 0.50$.

Furthermore, Yu *et al.* [50] recently reported that the introduction of a moderate oxygen vacancy concentration reduces the lattice thermal conductivity in SrTiO_3 [50]. Thus we can expect possibly enhanced scattering of phonons in the oxygen-deficient nickelate SLs which is crucial in optimizing the overall figure of merit (ZT). Hence exploring the thermoelectric response in $(\text{LaNiO}_{3-\delta})_1/(\text{LaAlO}_3)_1(001)$ SLs might provide useful insights in this direction.

To address these questions, in this work using DFT+ U calculations we explore the electronic and magnetic properties of $(\text{LaNiO}_{3-\delta})_1/(\text{LaAlO}_3)_1(001)$ SL ($\delta = 0.0-0.50$). We start with the electronic and structural properties of bulk LaNiO_3 to ensure that the confined monolayer of LaNiO_3 in $(\text{LaNiO}_3)_1/(\text{LaAlO}_3)_1(001)$ SL is under tensile strain at a_{STO} and compressive strain at a_{LSAO} . Next we turn to the pristine $(\text{LaNiO}_3)_1/(\text{LaAlO}_3)_1(001)$ SL. By using a larger lateral unit cell [51], we find the stabilization of an AFM-CD ($d^8\bar{L}^2$) $_{S=0}(d^8)_{S=1}$ phase and compare this with the metastable FM-CD phase at tensile (a_{STO}) and compressive (a_{LSAO}) strain, respectively. In addition, we obtain the lattice dynamic stability of the pristine $(\text{LaNiO}_3)_1/(\text{LaAlO}_3)_1(001)$ SL.

Furthermore, by varying the oxygen vacancy concentration in $(\text{LaNiO}_{3-\delta})_1/(\text{LaAlO}_3)_1(001)$ SL, we show that charge localization in conjunction with confinement and strain triggers an electronic reconstruction leading to a ferrimagnetic ordering at $\delta = 0.125$ and 0.25 , independent of strain. Moreover, at $\delta = 0.5$, an insulating phase emerges with alternating stripes of Ni^{2+} (high-spin) and Ni^{2+} (low-spin) and oxygen vacancies ordered along the [110] direction at both tensile and compressive strain. We also prove the lattice dynamic stability of this phase. Overall we find that the confinement induced MIT in $(\text{LaNiO}_{3-\delta})_1/(\text{LaAlO}_3)_1(001)$ SLs occurs independent of the oxygen vacancy concentration and strain.

Lastly, using Boltzmann transport theory within the constant relaxation time approximation, we show how oxygen

vacancies can be used to effectively tune the localization of Ni $3d$ states in ultrathin nickelate superlattices, subsequently impacting the thermoelectric response. At $\delta = 0.5$, a combination of flat and dispersive bands in the vicinity of the conduction band edge result in simultaneously high values of both the Seebeck coefficient and the electrical conductivity, together leading to a promising in-plane n -type power factor of $24 \mu\text{W}/\text{K}^2 \text{ cm}$ at a_{STO} and $14 \mu\text{W}/\text{K}^2 \text{ cm}$ at a_{LSAO} (assuming $\tau = 4$ fs) at 300 K. This can be compared with some of the best performing oxide thermoelectrics, such as La- or Nb-doped SrTiO_3 [52–54] or recent predictions for $\text{SrXO}_3/\text{SrTiO}_3(001)$ SLs, $X = \text{V, Cr, or Mn}$ [51,55].

II. COMPUTATIONAL DETAILS

First principles calculations for $\text{LaNiO}_{3-\delta}$ and $(\text{LaNiO}_{3-\delta})_1/(\text{LaAlO}_3)_1(001)$ SLs ($\delta = 0, 0.125, 0.25,$ and 0.5) were performed within the framework of spin-polarized DFT [56] using the Vienna *ab initio* simulation package (VASP) [57,58] with the projector augmented wave (PAW) basis [59,60]. The generalized gradient approximation was used for the exchange correlation functional in the implementation of Perdew, Burke, and Ernzerhof [61]. In order to take static correlation effects into account, the DFT+ U approach [62] with $U = 4$ eV for the Ni $3d$ and $U = 7$ eV for the La $4f$ was employed within Dudarev's scheme [63]. In addition, the effect of the Hubbard U term on the electronic and magnetic properties of $(\text{LaNiO}_3)_1/(\text{LaAlO}_3)_1(001)$ SLs was studied by optimizing the volume with a varying value of U_{Ni} from 1 to 5 eV in spin-polarized calculations. The role of La $4f$ states was assessed by carrying out calculations with $U_{\text{La}} = 0$ and 7 eV (see Sec. B of Appendix).

We model the 1/1 SLs by using laterally enlarged $2\sqrt{2}a \times 2\sqrt{2}a \times 2c$ supercells that contain 80 atoms in total [51]. To model epitaxial growth under tensile and compressive strain, we fixed the in-plane lattice constant to the experimental lattice constants of SrTiO_3 ($a_{\text{STO}} = 3.905 \text{ \AA}$) and LaSrAlO_4 ($a_{\text{LSAO}} = 3.756 \text{ \AA}$) reported in Ref. [32], respectively, whereas the c parameter along with the internal positions were fully optimized until the forces were less than 0.001 eV/\AA . To sample the Brillouin zone, we have used $5 \times 5 \times 6$ Monkhorst-Pack k points [64] for the 1/1 superlattices.

To confirm that the confined monolayer of LaNiO_3 in $(\text{LaNiO}_3)_1/(\text{LaAlO}_3)_1(001)$ SL is under tensile strain at a_{STO} and compressive strain at a_{LSAO} , a non-spin-polarized calculation was performed on bulk LaNiO_3 with PBEsol + U to simultaneously optimize the lattice parameters and the internal coordinates (volume-cell relaxation). The rhombohedral cell ($R\bar{3}c$, space group No. 167) in the hexagonal set up [65] was adopted, containing 30 atoms. A Γ centered k -mesh of $9 \times 9 \times 3$ was used.

To prove the dynamic stability of the ground state SL structure and magnetic order in $(\text{LaNiO}_3)_1/(\text{LaAlO}_3)_1(001)$ and $(\text{LaNiO}_{2.5})_1/(\text{LaAlO}_3)_1(001)$ SLs, respectively, lattice dynamics calculations were performed on the volume-cell relaxed structures (obtained with PBEsol+ U , $U_{\text{Ni}} = 4$ eV and $U_{\text{La}} = 7$ eV) using the supercell finite-differences approach implemented in the Phonopy

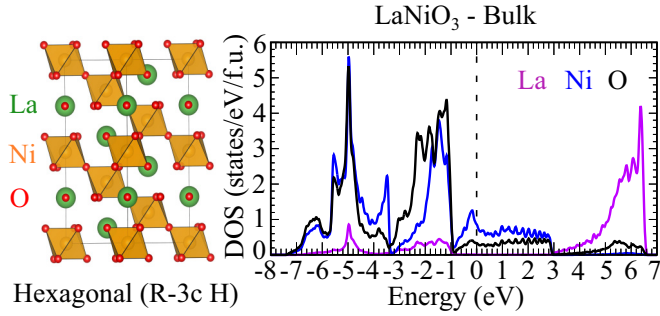


FIG. 1. (Left) Side view of the volume-cell relaxed hexagonal cell of bulk LaNiO_3 . (Right) Element resolved density of states (DOS) of bulk LaNiO_3 . Magenta, blue and black color represents the La, Ni, and O states, respectively.

package [66,67]. The second-order (harmonic) force constants were calculated using $1 \times 1 \times 1$ and $1 \times 1 \times 2$ supercells of the $(\text{LaNiO}_3)_1/(\text{LaAlO}_3)_1(001)$ SL and the $(\text{LaNiO}_{2.5})_1/(\text{LaAlO}_3)_1(001)$ SL leading to 60 and 116 displacements, respectively. Note that the supercells are with respect to the above mentioned $2\sqrt{2}a \times 2\sqrt{2}a \times 2c$ system. Atom-projected vibrational density of states curves were computed by interpolating the phonon frequencies on to a regular Γ centered q -point $15 \times 15 \times 18$ grid using the linear tetrahedron method for Brillouin zone integration. Phonon dispersions were obtained by evaluating frequencies at strings of q points along the high-symmetry points in the respective Brillouin zone by employing the SUMO package [68].

Lastly, we have calculated the thermoelectric properties employing Boltzmann transport theory in the constant relaxation time approximation, as implemented in the BOLTZTRAP code [69] using a very dense k mesh of $20 \times 20 \times 24$. For calculating the thermoelectric quantities we have utilized the approach of Sivan and Imry [70], described and used in previous studies [23,71,72].

III. ELECTRONIC AND STRUCTURAL PROPERTIES OF BULK LaNiO_3

We start by discussing the electronic and structural properties of bulk LaNiO_3 . From the volume-cell relaxed hexagonal structure of bulk LaNiO_3 (shown in Fig. 1, left), we obtained the pseudo-cubic lattice constant of 3.80 \AA which is in excellent agreement with the experimental value of 3.832 \AA at $T = 1.5 \text{ K}$ [65]. Noting the experimental lattice constants of bulk LaAlO_3 (3.792 \AA), SrTiO_3 (3.905 \AA), and LSAO (3.756 \AA), it is confirmed that the confined monolayer of LaNiO_3 in $(\text{LaNiO}_3)_1/(\text{LaAlO}_3)_1(001)$ SL is under tensile strain at a_{STO} and compressive strain at a_{LSAO} , respectively. The element-resolved density of states (DOS) in Fig. 1 (right), exhibits metallic behavior in agreement with the experimental findings [6]. The states between -1 to 3 eV are predominantly of Ni $3d$ character with lower contribution from O states, whereas Ni $3d$ states with prominent peaks, admixed with comparable O $2p$ states can be observed between -7 to -1 eV , indicating strong p - d hybridization. The La $4f$ states remain localized between 5 to 7 eV with $U_{\text{La}} = 7 \text{ eV}$.

IV. ELECTRONIC AND MAGNETIC PROPERTIES OF THE PRISTINE $(\text{LaNiO}_3)_1/(\text{LaAlO}_3)_1(001)$ SUPERLATTICE

To understand the interplay of confinement and strain, we now discuss the electronic and magnetic properties of the pristine SL. The optimized cross-plane lattice constants are 3.74 and 3.88 \AA at tensile and compressive strain, respectively. The partial occupation of the degenerate e_g orbitals is accommodated by charge disproportionation $(d^8\bar{L})(d^8\bar{L}) \rightarrow (d^8\bar{L}^2)_{S=0}(d^8)_{S=1}$, including both Ni and O in the NiO_6 octahedra, irrespective of strain. Similar to the low-temperature phase of $R\text{NiO}_3$ [17], the pristine $(\text{LaNiO}_3)_1/(\text{LaAlO}_3)_1(001)$ SL exhibits a “breathing-mode” distortion, which creates expanded ($S = 1$) and compressed ($S = 0$) NiO_6 octahedra with volume of 10.61 and 9 \AA^3 (a_{STO}) and 10 and 8.63 \AA^3 (a_{LSAO}) at the Ni1 and Ni2 sites [Fig. 2(a)], respectively, forming a two-dimensional checkerboard pattern. Notably, the Ni moments are arranged in a $\dots \uparrow \cdot 0 \cdot \downarrow \cdot 0 \dots$ pattern along the $[100]$ direction [see Fig. 2(b), left]. Such a confinement-induced electronic reconstruction leads to the opening of a band gap which is smaller under tensile strain (0.79 eV) than compressive strain (1 eV), along with a slightly enhanced Ni^{2+} spin magnetic moment ($1.48 \mu_B$) at tensile strain, compared to ($1.44 \mu_B$) at compressive strain.

At $a_{\text{STO}}/a_{\text{LSAO}}$, the AFM-CD $(d^8\bar{L}^2)_{S=0}(d^8)_{S=1}$ phase was found to be more stable than the FM-CD [22], stripe AFM-CD (S-AFM-CD), and G-AFM magnetic order by $17/11 \text{ meV/Ni atom}$, $49/24 \text{ meV/Ni atom}$, and $81/131 \text{ meV/Ni atom}$, respectively. Note that the S-AFM-CD magnetic order comprises alternating stripes of Ni moments having $\dots \uparrow \cdot 0 \cdot \uparrow \cdot 0 \dots$ and $\dots \downarrow \cdot 0 \cdot \downarrow \cdot 0 \dots$ pattern, along the $[\bar{1}10]$ direction, respectively. We compare the electronic and magnetic properties of the ground state AFM-CD phase with the metastable phases at both tensile and compressive strain. By analyzing the orbital-projected DOS for the AFM-CD phase in Fig. 2(c) for a_{STO} [see Fig. 7(c) in Sec. A of Appendix for a_{LSAO}], we observe that both e_g orbitals are nearly singly occupied and hybridized with apical oxygen states (orange filled curves), along with fully filled t_{2g} orbitals (d^8) below the Fermi level at the Ni1 sites. Furthermore, the basal oxygen is slightly spin-polarized ($\sim 0.03 \mu_B$), followed by a negligible spin polarization and a suppression of holes at the apical oxygens. On the other hand, in the Ni_2O_6 octahedra only the t_{2g} orbitals are filled in both spin channels, leading to a zero spin moment, along with predominantly depleted apical oxygen states (orange filled curves) below the Fermi level ($d^8\bar{L}^2$). Overall the confinement leads to an AFM-CD $(d^8\bar{L}^2)_{S=0}(d^8)_{S=1}$ phase, irrespective of strain, similar to the bulk rare-earth nickelates [17]. In the FM-CD phase, the charge disproportionation is somewhat less pronounced, reflected in distinct magnetic moments of $1.5/0.6 \mu_B$ (a_{STO}) and $1.43/0.54 \mu_B$ (a_{LSAO}) at the Ni1/Ni2 sites, shown in the spin density plot in Figs. 2 and 7 (see Appendix), respectively; consistent with previous studies [22,23]. We also find distinct breathing-mode distortions and magnetic moments for S-AFM-CD order: $1.55/0 \mu_B$ (a_{STO}) and $1.5/0 \mu_B$ (a_{LSAO}) with the corresponding octahedral volumes $10.7/9 \text{ \AA}^3$ (a_{STO}) and $10.13/8.64 \text{ \AA}^3$ (a_{LSAO}) at the Ni1/Ni2 sites, respectively. Interestingly, a similar magnetic ordering dependent breathing-mode distortion has been reported previously

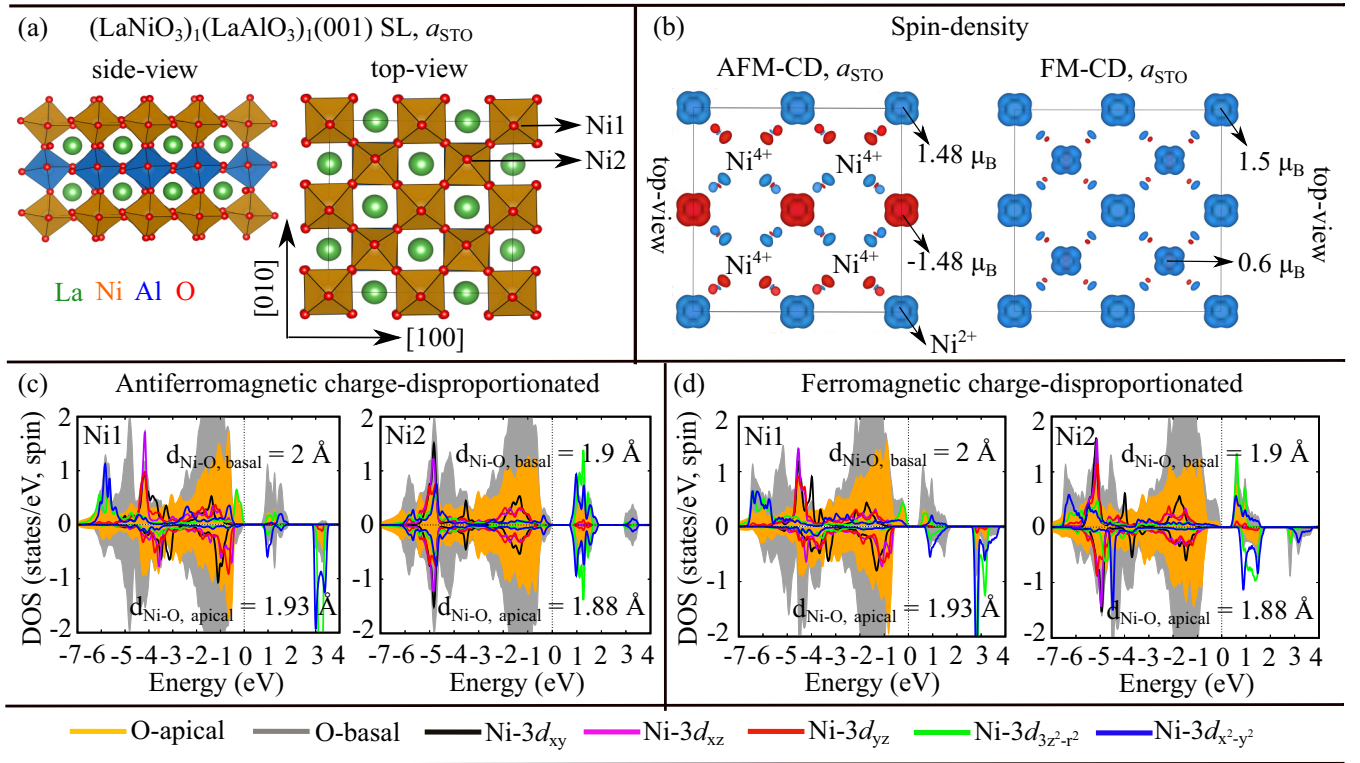


FIG. 2. (a) Side and top views of the optimized pristine $(\text{LaNiO}_3)_1/(\text{LaAlO}_3)_1(001)$ SL at a_{STO} , (b) Spin densities (side and top views), integrated from -7 eV to the Fermi energy (0 eV), together with the local magnetic moments at the two distinct Ni sites. Blue and red colors correspond to positive and negative spin densities, respectively. (c) Orbital-projected DOS of the two distinct Ni sites with (c) antiferromagnetic and (d) ferromagnetic coupling, along with the density of states of the apical and basal oxygen associated with their corresponding octahedra. The isovalue of the spin-density is $0.006 e/\text{\AA}^3$.

in bulk NdNiO_3 [73]. On the other hand, for G-AFM order, a uniform magnetic moment of $0.7 \mu_B$ was obtained at all Ni sites, irrespective of strain. This goes hand-in-hand with a depletion of states below the Fermi level of the apical $\text{O}2p$ states at all the octahedra, irrespective of strain (see Fig. 8 of Appendix). Our results highlight that the magnetic order and strain have direct impact on the degree of breathing-mode distortion in the pristine $(\text{LaNiO}_3)_1/(\text{LaAlO}_3)_1(001)$ SL. Finally, we have also studied the effect of Hubbard U at Ni $3d$ states on the electronic and magnetic properties of the pristine SLs (see Sec. B of Appendix). We adopted $U_{\text{Ni}} = 4$ eV in this work as it renders the charge-disproportionation in agreement with previous studies [22,23].

V. LATTICE DYNAMICAL STABILITY OF PRISTINE $(\text{LaNiO}_3)_1/(\text{LaAlO}_3)_1(001)$ SUPERLATTICE

In this section, we turn to the lattice dynamical stability of $(\text{LaNiO}_3)_1/(\text{LaAlO}_3)_1(001)$ SL in the AFM-CD $[(d^8L^2)_{S=0}(d^8)_{S=1}]$ phase. In contrast to the strained SLs considered in Sec. IV, here we have adopted the volume-cell relaxed SL structure, obtained by employing $U_{\text{Ni}} = 4$ eV and $U_{\text{La}} = 7$ eV, respectively. The optimized in-plane and cross-plane lattice parameters are 3.81 and 3.8 \AA , respectively. Using the laterally enlarged $2\sqrt{2}a \times 2\sqrt{2}a \times 2c$ cell in the AFM-CD phase, the symmetry reduced spontaneously from the monoclinic ($P2_1/c$) to triclinic ($P1$) symmetry, similar

to the strained SLs, considered in Sec. IV. From the layer-, element-, and spin-resolved DOS in Fig. 3 (left), it can be observed that the Ni $3d$ states lie in the band gap of LaAlO_3 , whereas the La $4f$ states lie between 6 and 7 eV. The electronic properties in the vicinity of the Fermi level are governed by the Ni $3d$ states admixed with O $2p$ states, with negligible contribution from La and Al states, respectively. The system has a band gap of 0.92 eV and a Ni^{2+} spin magnetic moment of $1.44 \mu_B$.

The vibrational density of states (VDOS) in Fig. 3 (right) exhibits no imaginary phonon frequencies, proving that the SL is dynamically stable. The La VDOS extends predominantly between 0 – 5 THz with the most prominent peak at 4 THz, constituting mainly the acoustic phonon modes along with a smaller contributions from oxygen. The O VDOS has four peaks between 5 – 20 THz. The Ni and Al VDOS are much lower, the former is more pronounced between 5 – 14 THz, while the latter between 7 – 17 THz. Notably, the Ni1 sites with half-filled e_g orbitals have a VDOS peak between 5 – 10 THz, whereas the VDOS of the Ni2 ions with fully filled t_{2g} orbitals shows four peaks with lower intensity between 5 – 20 THz. We further outline the essential role of the $1 \times 1 \times 2$ supercell in achieving the lattice dynamical stability in the pristine SL. Using the smaller $1 \times 1 \times 1$ supercell yielded finite imaginary phonon frequencies arising from the La ions, shown in Fig. 10(a) of the Appendix.

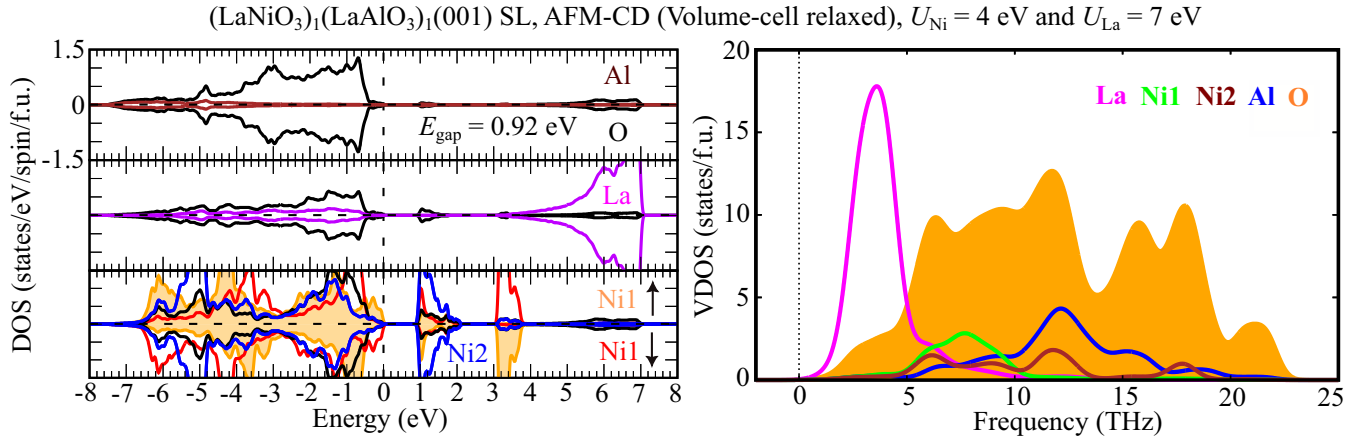


FIG. 3. Layer-, element-, and spin-resolved DOS (left panel) and corresponding element-projected vibrational density of states curves (right panel) of the volume-cell relaxed $(\text{LaNiO}_3)_1/(\text{LaAlO}_3)_1(001)$ SL with AFM-CD $[(d^8\bar{L}^2)_{S=0}(d^8)_{S=1}]$ magnetic order, obtained using $U_{\text{Ni}} = 4$ eV and $U_{\text{La}} = 7$ eV, respectively. In the projected density of states, magenta, black and brown color represent La, O, and Al states, respectively. Additionally in the NiO_2 panel, orange and red lines represent the spin-up and spin-down states, respectively, of the Ni1 $[(d^8)_{S=1}]$ sites, whereas, blue lines represent the PDOS of the Ni2 $[(d^8\bar{L}^2)_{S=0}]$ sites. The dashed vertical line at zero energy represents the Fermi level. In the vibrational density of states, magenta, green, brown, blue, and orange color represent La, Ni1, Ni2, Al, and O states, respectively.

VI. ELECTRONIC AND MAGNETIC PROPERTIES OF $(\text{LaNiO}_{3-\delta})_1/(\text{LaAlO}_3)_1(001)$ SUPERLATTICES

Here we discuss the influence of oxygen vacancies on the electronic and magnetic properties of $(\text{LaNiO}_{3-\delta})_1/(\text{LaAlO}_3)_1(001)$ SL. The oxygen vacancy concentration (δ) is varied from 0.125 to 0.5. The effect of strain is considered by setting the lateral lattice constant to bulk SrTiO_3 ($a_{\text{STO}} = 3.905$ Å) and LaSrAlO_4 ($a_{\text{LSAO}} = 3.756$ Å). The cross-plane lattice constants do not vary much with δ : 3.75–3.77 Å (a_{STO}) and 3.86–3.88 Å (a_{LSAO}).

At $\delta = 0.125$, we find that the oxygen vacancy (V_O) prefers to occupy the NiO_2 plane (see Table II in Sec. D 1 of Appendix), irrespective of strain, similar to findings for lower oxygen vacancy concentrations [49]. The orbital-projected DOS of all the Ni sites indicated in Fig. 4(a) is displayed in Fig. 15 of Appendix, at both tensile and compressive strain, respectively. The localization of electrons released by the oxygen defects triggers a varying degree of CD throughout the LaNiO_3 layer, resulting in distinct spin moments at the Ni sites, shown in the spin density plot in Fig. 4(a) for a_{STO} (see Fig. 15 of Appendix for a_{LSAO}). With one oxygen vacancy (1/4 electron per Ni site), the two released electrons localize at distant Ni sites (Ni6 and Ni7) from the oxygen defect site rather than on an adjacent Ni site, connected by green lines on the spin density plot in Fig. 4(a) for a_{STO} [see Fig. 15(b) of Appendix for a_{LSAO}]. The orbital-projected DOS of Ni6 and Ni7 show that both the e_g orbitals are occupied in the spin-up channel, irrespective of strain. This leads to enlarged octahedral volumes 10.76 Å³ (a_{STO})/ 9.94 Å³ (a_{LSAO}) and a spin magnetic moment of 1.55 μ_B (a_{STO})/ 1.46 μ_B (a_{LSAO}). Further sites with nonzero magnetic moments are Ni3 (1.1 μ_B), Ni4 (0.85 μ_B), Ni5 (-0.5 μ_B), and Ni8 (-0.5 μ_B), the corresponding polyhedral volumes are 10, 9.5, 4.8, and 9.4 Å³, respectively. A similar variation in CD is also obtained at compressive strain [see Fig. 15(b) of Appendix]. Overall, a ferrimagnetic (FIM) order arises due to the negative spin moments of Ni5 and

Ni8. This results in an enhanced bandwidth of the conduction band, especially in the spin-down channel and a band gap of 0.5 eV at a_{STO} and 0.32 eV at a_{LSAO} , respectively. Apart from the FIM-CD phase, we find an insulating AFM phase, 26 meV/Ni ion at a_{STO} and 27.5 meV/Ni ion at a_{LSAO} less stable than FIM-CD. The LDOS of the two magnetic phases at tensile and compressive strain are provided in Fig. 14, Sec. D 2 of Appendix. Furthermore, the relative stability of different possible magnetic configurations is displayed in Table III (for both tensile and compressive strain) and discussed in Sec. D 1 of Appendix. We find that one oxygen vacancy in the NiO_2 plane is 0.5 eV/SL more stable at a_{LSAO} than at a_{STO} , similar to results at lower oxygen vacancy concentrations and at different compressive strain ($a_{\text{LaAlO}_3} = 3.79$ Å) [49].

To determine the energetically favorable positions for the oxygen divacancies at $\delta = 0.25$ in the SLs, we placed the two V_O at all possible sites and relaxed the internal coordinates, while keeping the volume fixed to the optimized pristine SL, obtained at a_{STO} and a_{LSAO} , respectively. The relative total energies with respect to the most favorable configuration are displayed in Fig. 4(b) for a_{STO} [see Fig. 16(a) of Appendix for a_{LSAO}], we conclude that in the most favourable configuration the two oxygen vacancies are located in the NiO_2 plane along the $[110]$ direction at a distance of ≈ 4.1 Å at a_{STO} and ≈ 3.88 Å at a_{LSAO} . With on average 1/2 electron per Ni site, 3 out of 4 released electrons localize at Ni3, Ni6, and Ni7 sites, respectively, resulting in spin moments exceeding 1.5 μ_B , irrespective of strain. The fourth electron occupies the spin-down $d_{3z^2-r^2}$ orbital at the square-planar NiO_2 site, leading to a quenched spin magnetic moment of $-0.05\mu_B$, and a band gap opening due to the crystal field splitting between the e_g states, shown in the orbital-projected DOS [see Fig. 16(b) for a_{STO} and Fig. 16(c) for a_{LSAO} of Appendix]. Similar to $\delta = 0.125$, the localization of electrons released by oxygen defects in the NiO_2 plane leads to a FIM-CD phase, with three sites with negative Ni spin moment (Ni2, Ni4, and

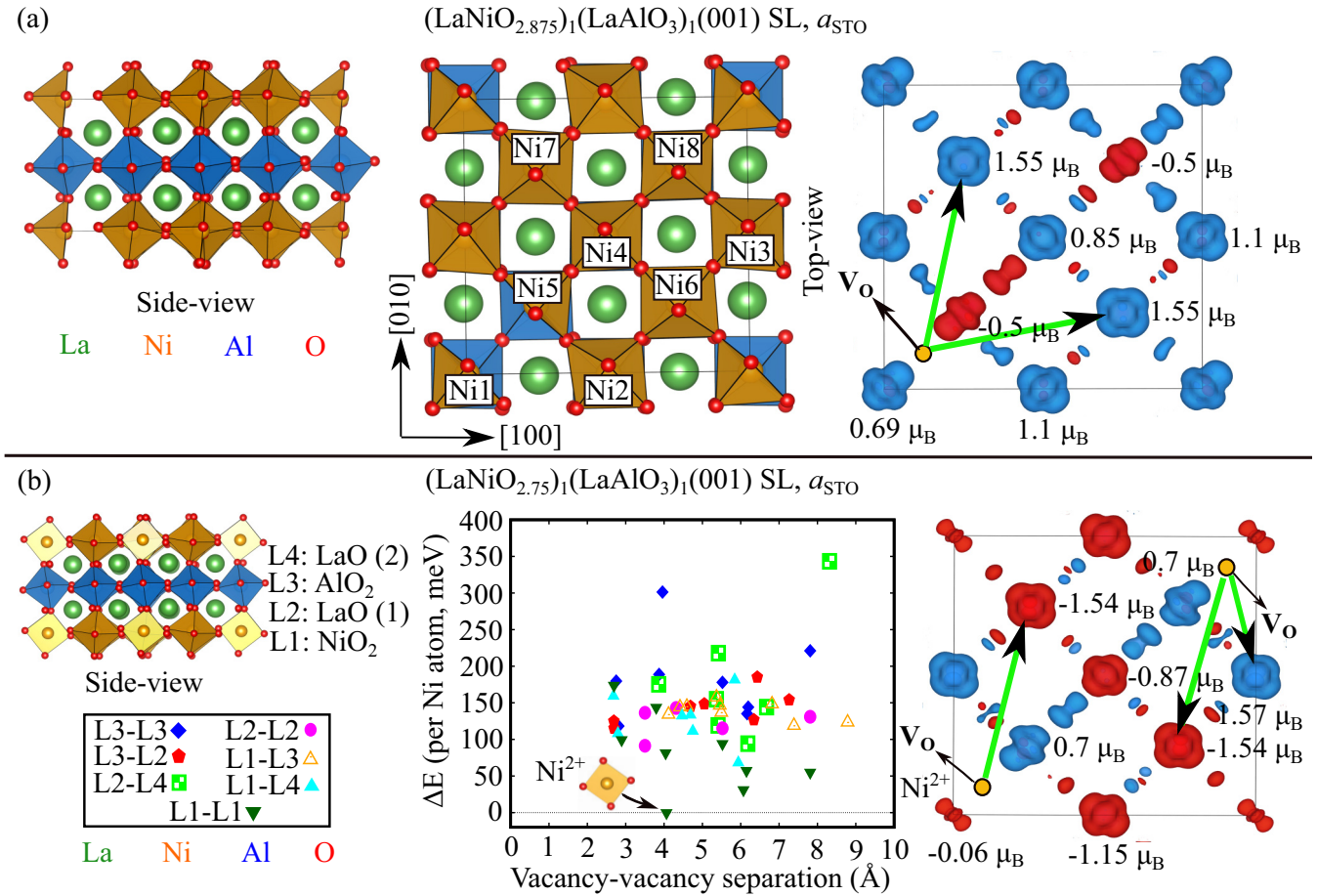


FIG. 4. (a) Side and top views of the optimized structure of $(\text{LaNiO}_{2.875})_1/(\text{LaAlO}_3)_1(001)$ SL and the corresponding spin-density plot at a_{STO} . Ni sites with distinct spin moments and symmetry inequivalence are marked on the top view of the optimized SL structure. (b) Relative energy difference of all possible configurations for two oxygen vacancies in a $(\text{LaNiO}_{2.75})_1/(\text{LaAlO}_3)_1(001)$ SL at a_{STO} . ΔE with respect to the most stable configuration as a function of the distance between the vacancies. The spin-density of the lowest energy case with Ni²⁺ (LS) site in a fourfold coordination at a_{STO} is displayed on the right. L1 to L4 denote the planes in the SL. Li-Lj indicates in which layer the two vacancies are located (right). Blue and red colors denote positive and negative spin densities, respectively, integrated between -7 eV and the Fermi level. Green arrows connect the oxygen vacancy sites and the localization sites for the released electrons from the oxygen vacancy. The isovalue of the spin density is $0.006 \text{ e}/\text{\AA}^3$.

Ni6), as shown in the spin density plot in Fig. 4(b) for a_{STO} [see Fig. 16(a) of Appendix for a_{LSAO}]. A band gap of 0.6 eV at a_{STO} and 0.32 eV at a_{LSAO} emerges. Notably, the insulating FIM-CD phase, obtained in $(\text{LaNiO}_{2.75})_1/(\text{LaAlO}_3)_1(001)$ SL is distinct from the zigzag type AFM order with narrow band gap in $\text{LaNiO}_{2.75}$ bulk (DFT+ U) [46]. Finally, all other possible initial configurations resulted in ferrimagnetic order, albeit less stable, at both tensile and compressive strain.

At $\delta = 0.5$, guided by the $\delta = 0.25$ case, we find that the four oxygen vacancies order along the $[110]$ direction to form four NiO₄ plaquettes with square-planar geometry, as shown in Fig. 5(a). All other possible arrangements of the oxygen vacancies were found to be energetically less stable (see Sec. D 1 of Appendix), irrespective of strain. Out of the eight released electrons, four electrons occupy the spin-down $d_{3z^2-r^2}$ orbital at Ni1, Ni4, Ni5, and Ni8 in the square-planar plaquettes, leading to Ni²⁺ (LS), with a nominal magnetic moment of $\sim 0.1 \mu_B$, irrespective of strain, as shown in the orbital-projected DOS in Fig. 5 for a_{STO} [see Fig. 17(c) of

Appendix for a_{LSAO}]. The remaining four electrons localize at Ni2, Ni3, Ni6, and Ni7, resulting in an increased spin magnetic moment of $1.63 \mu_B$ (a_{STO}) and $1.60 \mu_B$ (a_{LSAO}) due to the half-filled e_g orbitals, corresponding to Ni²⁺ (HS). Together they form stripes along the $[110]$ direction of alternating Ni²⁺ (HS) in octahedral coordination and Ni²⁺ (low-spin) in a fourfold planar configuration. This S-AFM order results in a significantly reduced Ni $3d$ bandwidth and a larger band gap of 1.81 eV at a_{STO} and 1.65 eV at a_{LSAO} [see Fig. 18 for a_{STO} and Fig. 19 for a_{LSAO} of Appendix]. Interestingly, the Ni spins couple antiferromagnetically along the Ni²⁺ (HS) stripe, as shown in the spin density plot in Fig. 5(c). Notably, this is different from the A-type AFM order with a checkerboard ordering of NiO₄ and NiO₆ columns on the $(001)_{\text{pc}}$ plane in bulk $\text{LaNiO}_{2.5}$ [46]. The relative stability of different magnetic configurations is discussed in Sec. D 1 of Appendix for both tensile and compressive strain. From the above discussion, we conclude that the electron localization is the preferred mechanism to accommodate the excess

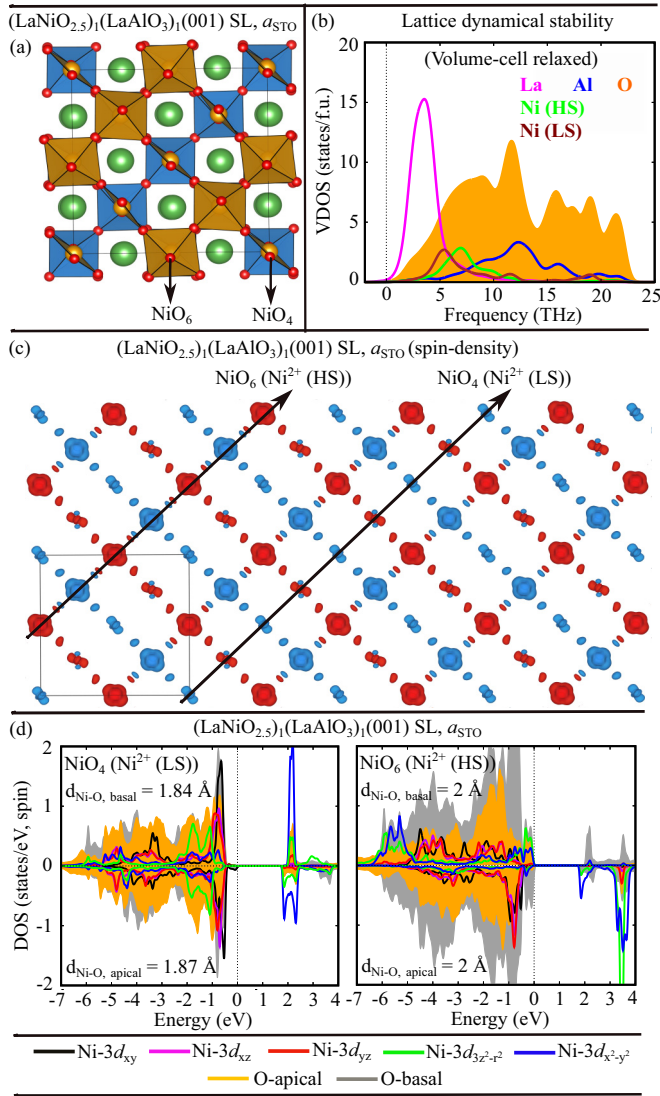


FIG. 5. (a) Top view of the optimized $(\text{LaNiO}_{2.5})_1/(\text{LaAlO}_3)_1(001)$ SL at a_{STO} . (b) Atom-projected vibrational density of states of the volume-cell relaxed $(\text{LaNiO}_{2.5})_1/(\text{LaAlO}_3)_1(001)$ SL with stripe AFM magnetic order, obtained using $U = 4$ eV on the Ni $3d$ and $U = 7$ eV on the La $4f$ states, respectively. In the vibrational density of states, magenta, green, brown, blue and orange colors represent La, Ni (HS), Ni (LS), Al, and O states, respectively. (c) Spin density integrated between -7 eV up to the Fermi level of the optimized $(\text{LaNiO}_{2.5})_1/(\text{LaAlO}_3)_1(001)$ SL at a_{STO} with isovalence $0.006 e/\text{\AA}^3$. Blue and red colors correspond to positive and negative spin densities, respectively. (d) The orbital projected density of states of the Ni^{2+} (LS), left and Ni^{2+} (HS), right, respectively, along with the density of states of the apical and basal oxygen associated with the NiO_4 square planar plaquette (left) and the NiO_6 octahedron (right).

electrons released from the oxygen vacancies, leading to MIT in $(\text{LaNiO}_{3-\delta})_1/(\text{LaAlO}_3)_1(001)$ SLs, irrespective of strain.

We now turn to the lattice dynamic stability of $(\text{LaNiO}_{2.5})_1/(\text{LaAlO}_3)_1(001)$ SL in the S-AFM phase. Here also, we adopted the volume-cell relaxed structure. The element-resolved VDOS shown in Fig. 5(b) exhibits no imaginary phonon frequencies and confirms the lattice dynamical

TABLE I. Thermoelectric performance of the $(\text{LaNiO}_{3-\delta})_1/(\text{LaAlO}_3)_1(001)$ SLs at different δ in comparison to a selection of prominent oxide thermoelectrics at room temperature (300 K).

System	S ($\mu\text{V}/\text{K}$)	PF ($\mu\text{W}/\text{K}^2 \text{ cm}$)
Tensile strain (a_{STO}), $\tau = 4$ fs		
$(\text{LaNiO}_3)_1/(\text{LaAlO}_3)_1(001)$		
in-plane (xx)	-418	10
cross-plane (zz)	-507	0.4
$(\text{LaNiO}_{2.875})_1/(\text{LaAlO}_3)_1(001)$		
in-plane (xx)	-518	9.4
cross-plane (zz)	-441	0.6
$(\text{LaNiO}_{2.75})_1/(\text{LaAlO}_3)_1(001)$		
in-plane (xx)	-393	0.2
cross-plane (zz)	-344	0.3
$(\text{LaNiO}_{2.5})_1/(\text{LaAlO}_3)_1(001)$		
in-plane (xx)	-467	24
cross-plane (zz)	-399	0.04
Compressive strain (a_{LSAO}), $\tau = 4$ fs		
$(\text{LaNiO}_3)_1/(\text{LaAlO}_3)_1(00)$		
in-plane (xx)	-546	19.5
cross-plane (zz)	-511	3.7
$(\text{LaNiO}_{2.875})_1/(\text{LaAlO}_3)_1(001)$		
in-plane (xx)	-461	4.5
cross-plane (zz)	-417	0.3
$(\text{LaNiO}_{2.75})_1/(\text{LaAlO}_3)_1(001)$		
in-plane (xx)	-470	0.6
cross-plane (zz)	-392	0.2
$(\text{LaNiO}_{2.5})_1/(\text{LaAlO}_3)_1(001)$		
in-plane (xx)	-400	14
cross-plane (zz)	-428	1.6
Literature		
SrTiO_3 (DFT [74], $\tau = 4.3$ fs)	-400	10
La: SrTiO_3 bulk, exp. [53]	-380	35
La: SrTiO_3 films, exp. [52]	-980	39
Nb: SrTiO_3 bulk, exp. [54]	-240	20

stability of the SL. Similar to the pristine SL case, the acoustic phonon modes with a peak at ~ 3 THz have La character admixed with lower contribution from O VDOS between 0–5 THz. Notably the O VDOS peaks, lying between 0–23 THz, differ from ones in the pristine SL, shown in Fig. 3. The Ni^{2+} (HS) and Ni^{2+} (LS) VDOS extend between 3–12 THz, the latter slightly shifted to lower frequencies, while the Al VDOS lies between 5–20 THz. For the lattice dynamical stability it was essential to employ a $1 \times 1 \times 2$ supercell (152 atoms). The $1 \times 1 \times 1$ supercell containing 76 atoms yielded instead finite imaginary phonon frequencies arising from the La atoms, shown in Fig. 10(b) of Appendix.

VII. THERMOELECTRIC PROPERTIES OF $(\text{LaNiO}_{3-\delta})_1/(\text{LaAlO}_3)_1(001)$ SUPERLATTICES

Finally, in this section, we discuss the thermoelectric properties of $(\text{LaNiO}_{3-\delta})_1/(\text{LaAlO}_3)_1(001)$ SLs at tensile and compressive strain, respectively, and compare them with other promising oxide thermoelectrics. We focus here on the n -type thermoelectric response. The thermoelectric

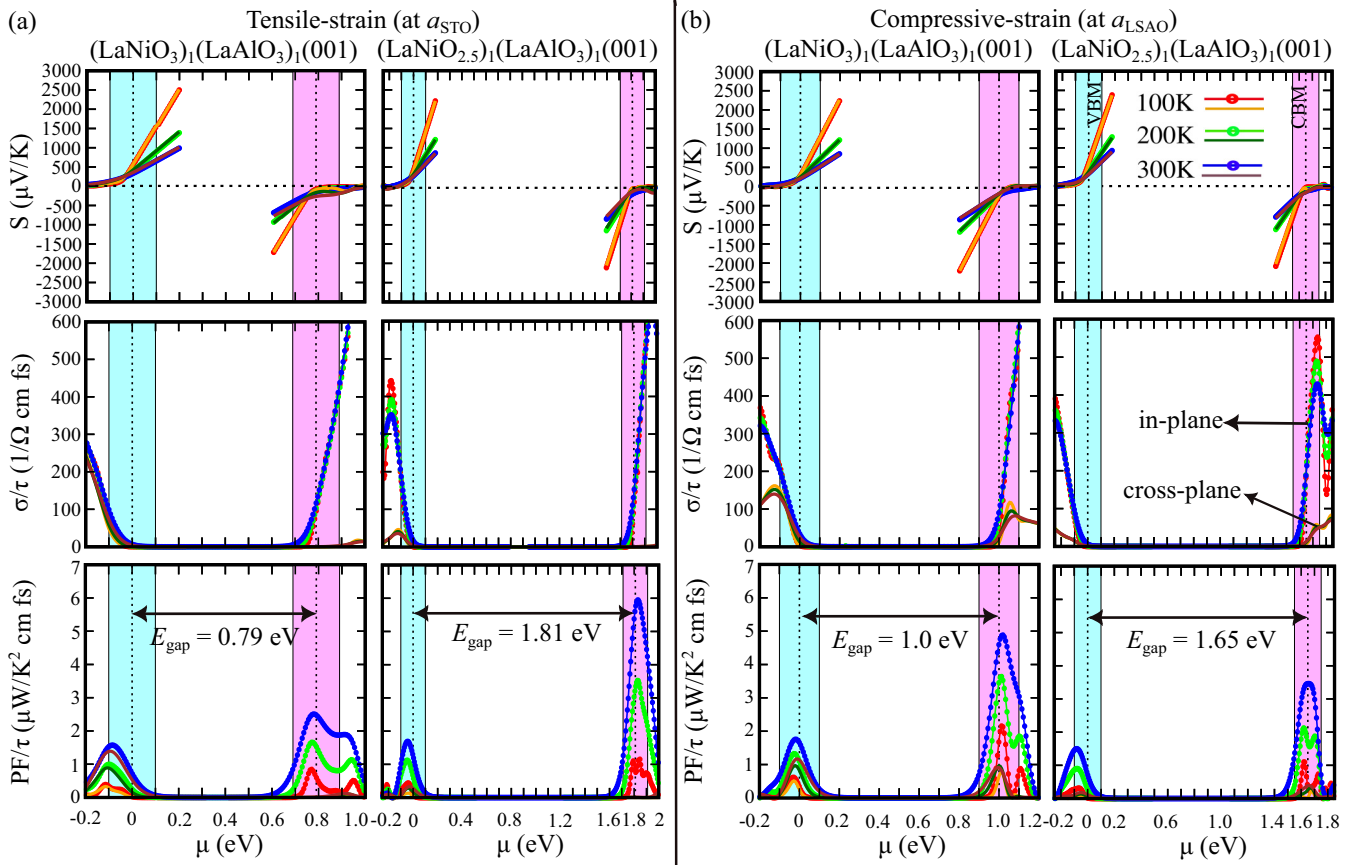


FIG. 6. Thermoelectric properties of $(\text{LaNiO}_{3-\delta})_1/(\text{LaAlO}_3)_1(001)$ SL ($\delta = 0$ and 0.5) at (a) a_{STO} and (b) a_{LSAO} , for three different temperatures 100, 200, and 300 K. (From top to bottom) Seebeck coefficient S , electrical conductivity σ/τ , and the electronic power factor PF/τ are shown, where τ denotes the relaxation time. Orange, dark-green, and brown lines (red, green, and blue dotted lines) correspond to cross-plane (in-plane) transport. The vertical dashed lines denote the VBM and CBM. The energy range where the chemical potential is varied (± 100 meV around VBM and CBM) is marked in cyan and magenta, respectively.

properties are summarized in Fig. 6 and Table I. We report power factors divided by the relaxation time PF/τ in Fig. 6 which are hence independent of the choice of τ and related to the electronic fitness function introduced by Xing *et al.* [75]. For Table I, we use a room-temperature relaxation time of $\tau = 4$ fs, a typical value for oxides [74]. In our discussion we focus on a variation of the chemical potential (μ) within a physically relevant ± 100 meV interval around the band edges, highlighted with cyan and magenta around the valence (VBM) and conduction band minimum (CBM), respectively, for the calculation of the Seebeck coefficient. With the chemical potential shifted to the CBM we obtain an estimate for the n -type thermoelectric response at 300 K. In the pristine SL at a_{STO} , the combination of flat and dispersive bands at the CBM leads to an in-plane electrical conductivity of $117 \text{ S cm}^{-1} \text{ fs}^{-1}$ (at E_F), which together with the high Seebeck coefficient reaching up to $-418 \text{ } \mu\text{V/K}$ (in-plane) results in a power factor of $10 \text{ } \mu\text{W/K}^2 \text{ cm}$ (assuming a relaxation time $\tau = 4$ fs). On the other hand, at a_{LSAO} , the bands at the CBM are relatively flat which leads to a reduced in-plane electrical conductivity of $90 \text{ S cm}^{-1} \text{ fs}^{-1}$, but a higher Seebeck coefficient reaching up to $-546 \text{ } \mu\text{V/K}$ (in-plane) giving rise to a higher power factor of $19.5 \text{ } \mu\text{W/K}^2 \text{ cm}$ than at a_{STO} .

For $\delta = 0.125$ and especially for 0.25 , the presence of localized flat bands at the CBM, results in appreciably high in-plane Seebeck coefficient, irrespective of strain, albeit lower than the corresponding values in the pristine SLs. However, the low values of the electrical conductivity (especially at $\delta = 0.25$) lead to very low power factors (see Table I and Fig. 20 of Appendix). Interestingly, for $\delta = 0.5$ at a_{STO} , the combination of flat and dispersive bands in the vicinity of the CBM results in a high in-plane electrical conductivity of $131 \text{ S cm}^{-1} \text{ fs}^{-1}$ which together with a high Seebeck coefficient reaching up to $-467 \text{ } \mu\text{V/K}$ (in-plane) leads to a robust power factor of $24 \text{ } \mu\text{W/K}^2 \text{ cm}$ (assuming a relaxation time $\tau = 4$ fs); more than twice compared to the pristine SL at 300 K. In contrast, for $\delta = 0.5$ at a_{LSAO} , the bands in the vicinity of the CBM are more dispersive which results in a much higher in-plane electrical conductivity of $187 \text{ S cm}^{-1} \text{ fs}^{-1}$ but a reduced Seebeck coefficient of up to $-400 \text{ } \mu\text{V/K}$ (in-plane). This leads to a lower power factor of $14 \text{ } \mu\text{W/K}^2 \text{ cm}$ than at a_{STO} . Overall, the thermoelectric power-factor in $(\text{LaNiO}_{3-\delta})_1/(\text{LaAlO}_3)_1(001)$ SLs especially at tensile strain is higher than in the pristine SLs, which makes the oxygen-deficient SLs attractive for thermoelectric applications. Moreover, the introduction of a moderate oxygen-vacancy concentration turns out to be

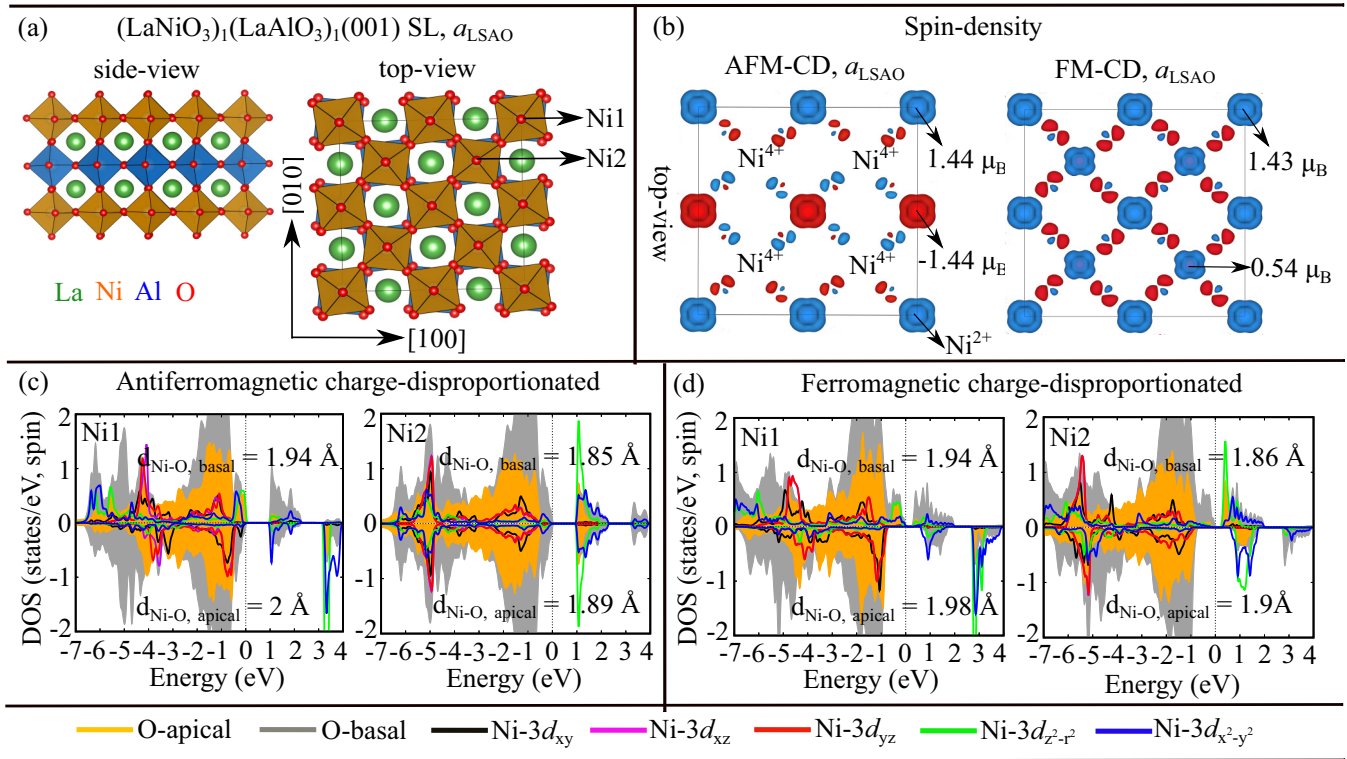


FIG. 7. (a) Side and top views of the optimized pristine (LaNiO₃)₁/(LaAlO₃)₁(001) SL at a_{LSAO} . (b) Spin densities of the AFM and FM-CD phases, integrated from -7 eV to the Fermi energy (0 eV), together with the local magnetic moments at the two distinct Ni sites. Blue and red colors correspond to positive and negative spin densities, respectively. [(c) and (d)] Orbital-projected DOS of the two distinct Ni sites in the antiferromagnetic and ferromagnetic charge-disproportionated phase, respectively, along with the density of states of the apical and basal oxygen associated with their octahedra. The isovalue of the spin-density is 0.006 e/Å³.

favorable for reducing the lattice thermal conductivity, as reported for SrTiO₃ [50].

VIII. SUMMARY

In summary, using a combination of DFT+ U and Boltzmann transport theory calculations in the constant relaxation time approximation, we studied the electronic, magnetic and thermoelectric properties of (LaNiO_{3- δ)₁/(LaAlO₃)₁(001) SLs for $\delta = 0, 0.125, 0.25,$ and 0.5 under tensile (a_{STO}) and compressive strain (a_{LSAO}). In the pristine 1/1 SLs, we found that confinement leads to an antiferromagnetic charge-disproportionated (AFM-CD) (d^8L^2) _{$S=0$} (d^8) _{$S=1$} phase, irrespective of strain. At $\delta = 0.125$ and 0.25 , the localization of electrons released by oxygen defect(s) in the NiO₂ plane results in semiconducting ferrimagnetic charge-disproportionated (FIM-CD) phases at both tensile and compressive strain. At $\delta = 0.5$, an insulating phase emerges with alternating stripes of octahedrally coordinated Ni²⁺ (HS) and Ni²⁺ (LS) in a square-planar geometry and oxygen vacancies ordered along the [110] direction (S-AFM), leading to a robust n -type in-plane power factor of 24 $\mu\text{W}/\text{K}^2$ cm at a_{STO} and 14 $\mu\text{W}/\text{K}^2$ cm at a_{LSAO} , respectively, (assuming a relaxation time $\tau = 4$ fs), at 300 K. In addition, the lattice dynamic stability was demonstrated for the pristine SL and for $\delta = 0.5$. These findings suggest ways to design exotic phases}

using oxygen vacancies in ultrathin nickelate superlattices, that are potentially interesting for applications.

ACKNOWLEDGMENTS

This work was supported by the German Research Foundation (Deutsche Forschungsgemeinschaft, DFG) within the CRC/TRR 80 (Project No. 107745057, subprojects G3 and

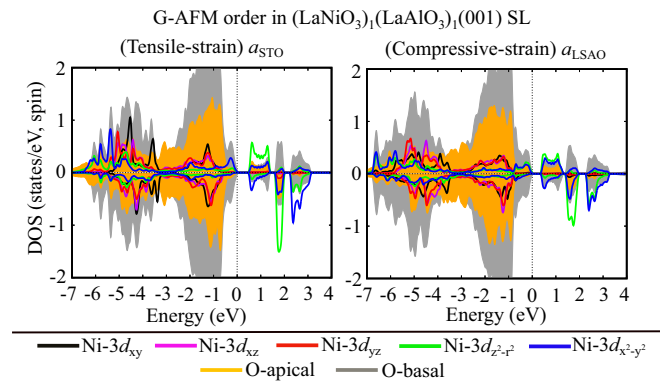


FIG. 8. Orbital projected density of states (OP-PDOS) of the Ni sites in (LaNiO₃)₁/(LaAlO₃)₁(001) SL with G-AFM order, also shown is the density of states of the apical and basal oxygen associated with the corresponding polyhedra in tensile and compressive strain.

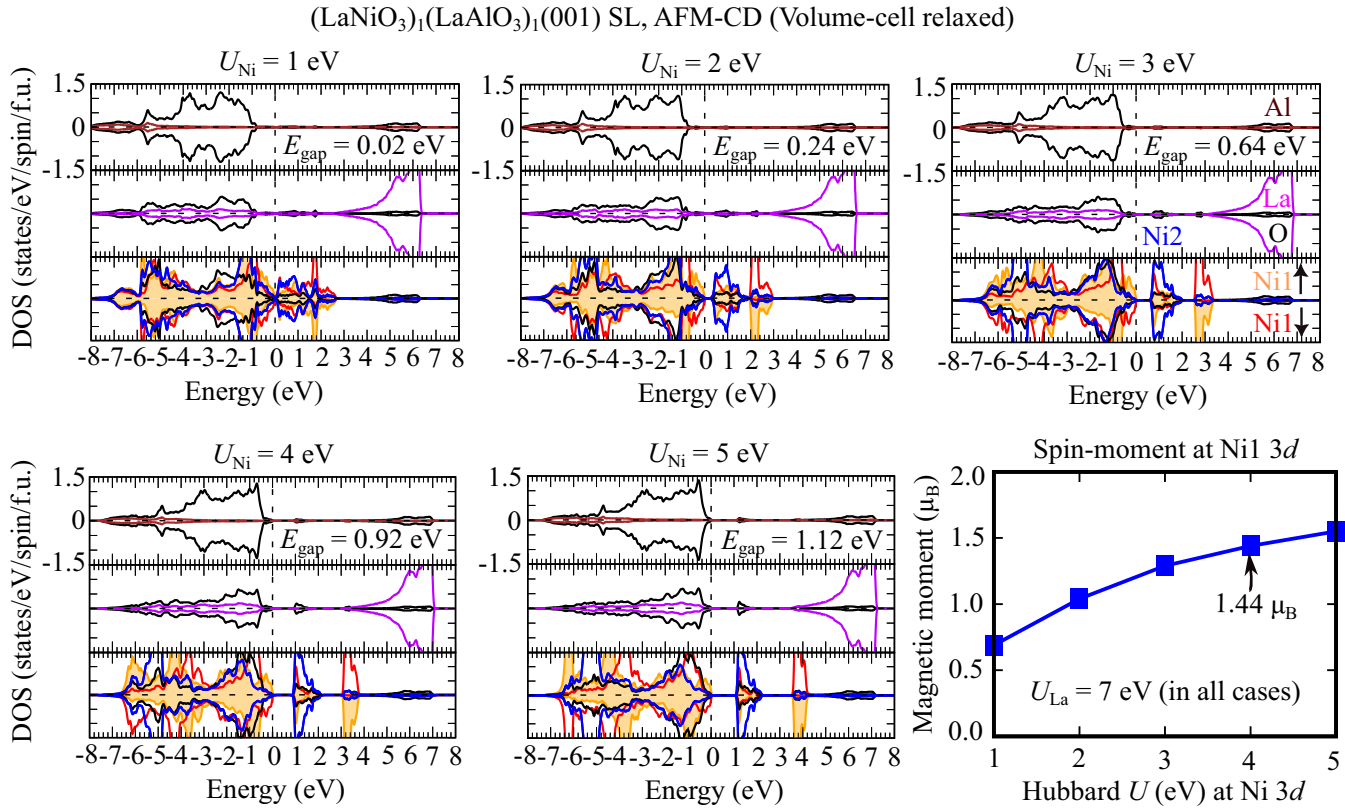


FIG. 9. Layer-, element-, and spin-resolved densities of states for the volume-cell relaxed (LaNiO₃)₁/(LaAlO₃)₁(001) SL with AFM-CD magnetic order, obtained using $U_{\text{Ni}} = 1, 2, 3, 4,$ and 5 eV, respectively. Note that $U_{\text{La}} = 7$ eV has been used in all cases. In the projected density of states, magenta, black, and brown color represent La, O, and Al states, respectively. Additionally in the NiO₂ panel, filled orange and red curves represent the spin-up and spin-down states, respectively, of the Ni1 atom, whereas, blue line represents the spin-polarized states of the Ni2 atom. The Fermi level is denoted by a dashed line at zero energy. Also shown is the spin magnetic moment at Ni1 3d site versus Hubbard U_{Ni} plot.

G8) and CRC/TRR247 (Project No. 388390466, B04). We acknowledge computational time at the Leibniz Rechenzentrum Garching, Project No. pr87ro and magnetUDE supercomputer

(DFG Grants No. INST 20876/209-1 FUGG and No. INST 20876/243-1 FUGG). We acknowledge support by the Open Access Publication fund of the University of Duisburg-Essen.

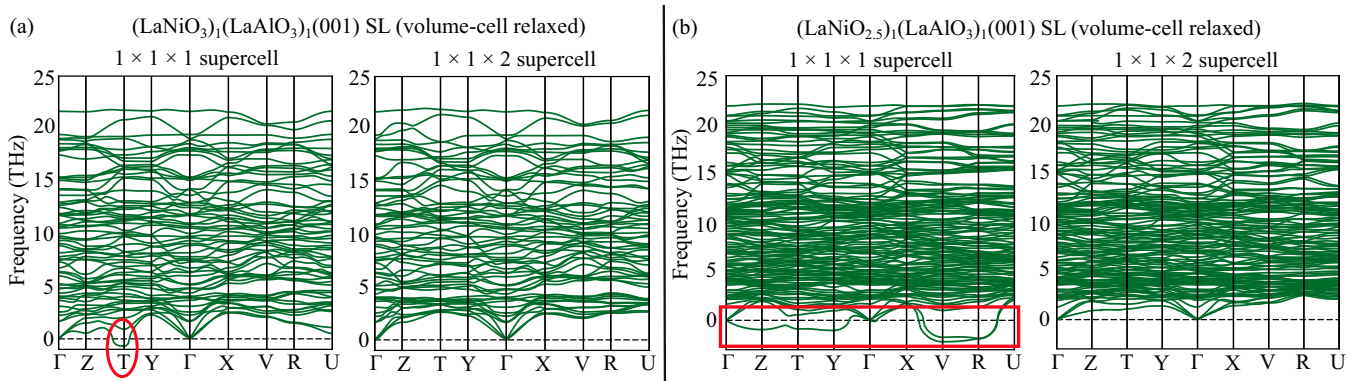


FIG. 10. (a) Phonon dispersion curves of the volume-cell relaxed (LaNiO₃)₁/(LaAlO₃)₁(001) SL with AFM-CD $[(d^8L^2)_{S=0}(d^8)_{S=1}]$ magnetic order ($U = 4$ eV at Ni 3d and 7 eV at La 4f states) by employing $1 \times 1 \times 1$ supercell containing 80 atoms (left) and $1 \times 1 \times 2$ supercell containing 160 atoms (right), respectively. (b) Phonon dispersion curves of the volume-cell relaxed (LaNiO_{2.5})₁/(LaAlO₃)₁(001) SL with stripe-AFM order (see Fig. 5 in the paper) by employing $1 \times 1 \times 1$ supercell containing 76 atoms (left) and $1 \times 1 \times 2$ supercell containing 152 atoms (right), respectively.

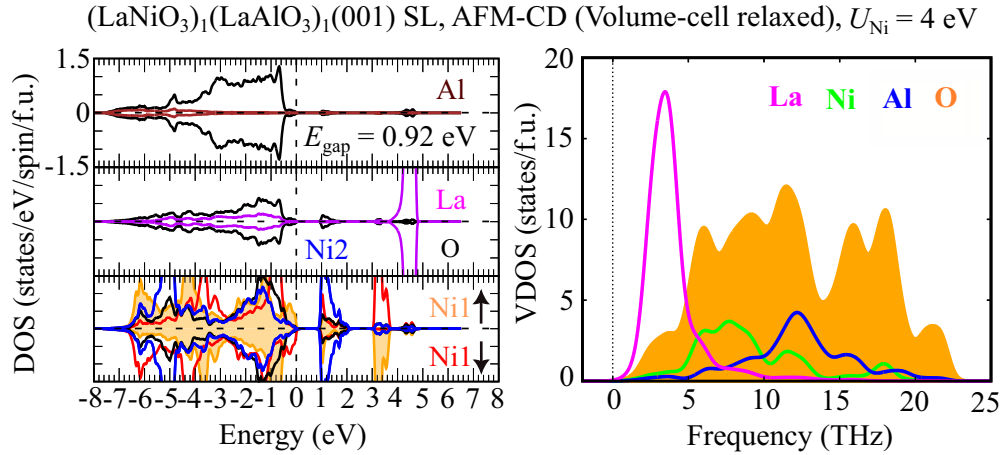


FIG. 11. Layer-, element-, and spin-resolved DOS (left panel) and corresponding element projected vibrational density of states curves (right panel) of the volume-cell relaxed $(\text{LaNiO}_3)_1/(\text{LaAlO}_3)_1(001)$ SL with AFM-CD $[(d^8\bar{L}^2)_{S=0}(d^8)_{S=1}]$ magnetic order, obtained using $U_{\text{Ni}} = 4$ eV and $U_{\text{La}} = 0$ eV, respectively. In the projected density of states, magenta, black and brown color represent La, O, and Al states, respectively. Additionally in the NiO_2 panel, filled orange and red curves represent the spin-up and spin-down states, respectively, of the Ni1 $[(d^8)_{S=1}]$ atom, whereas, blue line represents the spin-polarized states of the Ni2 $[(d^8\bar{L}^2)_{S=0}]$ atom. The dashed vertical line at zero energy represents the Fermi level. In the vibrational density of states, magenta, green, blue and orange color represent La, Ni, Al, and O states, respectively.

APPENDIX A: ELECTRONIC AND MAGNETIC PROPERTIES OF $(\text{LaNiO}_3)_1/(\text{LaAlO}_3)_1(001)$ SUPERLATTICES

The comparison of the electronic and magnetic properties of the AFM-CD and FM-CD phases in $(\text{LaNiO}_3)_1/(\text{LaAlO}_3)_1(001)$ SL at a_{LSAO} is shown in Fig. 7. The orbital projected density of states of the Ni sites with G-AFM order together with the density of states of the apical and basal oxygen in the pristine SLs at tensile and compressive strain is shown in Fig. 8.

APPENDIX B: EFFECT OF HUBBARD U ON THE ELECTRONIC AND MAGNETIC PROPERTIES OF $(\text{LaNiO}_3)_1/(\text{LaAlO}_3)_1(001)$ SUPERLATTICES

In this section we study the effect of Hubbard U at the Ni $3d$ orbitals on the electronic and magnetic properties of the pristine SL. Note that we have adopted the volume-cell relaxed structures at each U to subsequently analyze the electronic and magnetic properties. From the LDOS, obtained at $U_{\text{Ni}} = 1$ eV, it can be observed that the Ni $3d$ states split and form a band gap of 20 meV (Fig. 9). With increasing U_{Ni} value, the band gap increases, as shown in Fig. 9. On the other hand, the bandwidth of Ni $3d$ states admixed with O $2p$ states

TABLE II. Stabilization energy $[\Delta E = E(\text{oxygen vacancy in LaO or AlO}_2\text{-plane}) - E(\text{oxygen vacancy in NiO}_2\text{-plane})]$ per Ni atom] of $(\text{LaNiO}_{2.875})_1/(\text{LaAlO}_3)_1(001)$ SL at a_{STO} and a_{LSAO} , respectively.

Plane	ΔE at a_{STO} (meV per Ni atom)	ΔE at a_{LSAO} (meV per Ni atom)
LaO-plane	29	69
AlO ₂ -plane	55	54

reduces with increasing U_{Ni} value in both the valence and conduction bands, respectively. Interestingly, a gradual rigid upward shift is observed in the La $4f$ states with increasing U value at Ni $3d$ states. Finally, the Ni1 $3d$ magnetic moment was found to increase and saturate at $1.5 \mu_{\text{B}}$ with increasing U_{Ni} value.

APPENDIX C: LATTICE DYNAMICAL STUDY OF $(\text{LaNiO}_{3-\delta})_1/(\text{LaAlO}_3)_1(001)$ SUPERLATTICES, $\delta = 0$ AND 0.5

In this section, we discuss the lattice dynamical stability of the $(\text{LaNiO}_3)_1/(\text{LaAlO}_3)_1(001)$ SL with AFM-CD magnetic order and $(\text{LaNiO}_{2.5})_1/(\text{LaAlO}_3)_1(001)$ SL with S-AFM magnetic order. Figure 10 highlights the importance of using the $1 \times 1 \times 2$ supercell in achieving the lattice dynamical stability. In contrast the $1 \times 1 \times 1$ supercell leads to finite imaginary phonon frequencies, arising from La atoms (marked

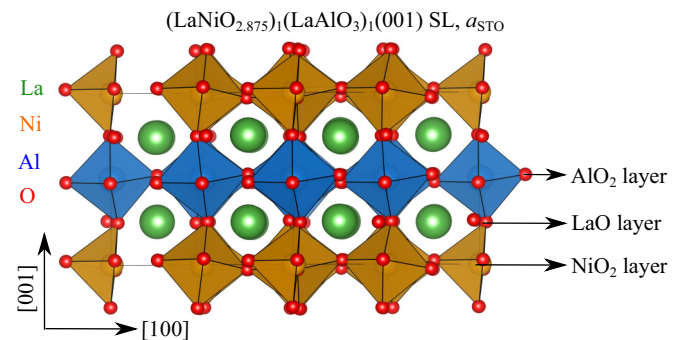


FIG. 12. Side view of the optimized $(\text{LaNiO}_{2.875})_1/(\text{LaAlO}_3)_1(001)$ SL with octahedral tilts and rotations. The atomic planes are marked on the right. The single oxygen vacancy is indicated by a missing basal oxygen atom in the NiO_2 plane.

TABLE III. Energy difference of various magnetic configuration with respect to the FiM ground state, $\Delta E = E(\text{MO}) - E(\text{FiM})$ per Ni atom, of $(\text{LaNiO}_{2.875})_1/(\text{LaAlO}_3)_1(001)$ SL at a_{STO} and a_{LSAO} , respectively. FiM is ferrimagnetic order whereas S-type AFM order denotes a stripe-like arrangement of ferro/antiferromagnetic Ni spins along $[\bar{1}10]$ direction.

Magnetic order (MO)	ΔE at a_{LSAO} (meV per Ni atom)	ΔE at a_{LSAO} (meV per Ni atom)
FM	24	34
G-AFM	83	105
S-AFM	26	27.5

in red) in both the cases. Next, we discuss the electronic and magnetic properties along with the lattice dynamic stability of $(\text{LaNiO}_3)_1/(\text{LaAlO}_3)_1(001)$ SL in the AFM-CD $[(d^8\bar{L}^2)_{S=0}(d^8)_{S=1}]$ phase, obtained using $U_{\text{Ni}} = 4$ eV ($U_{\text{La}} = 0$ eV). The optimized in-plane/cross-plane lattice parameters are 3.79 Å/3.78 Å, respectively. From the layer-, element-, and spin-resolved density of states in Fig. 11 (left), it can be observed that the electronic properties remains qualitatively unchanged, compared to $U_{\text{La}} = 7$ eV case (see Sec. V), except La 4*f* states which lie between 4 and 5 eV. Further, an electronic band gap of 0.92 eV along with the Ni^{2+} spin magnetic moment of 1.44 μ_{B} were obtained. The vibrational density of states (VDOS) in Fig. 11 (right) exhibits no imaginary phonon frequencies, proving that the SL is dynamically stable. Thus, we conclude that the electronic, magnetic, and the lattice dynamical stability are not influenced by the choice of U at the La 4*f* states.

APPENDIX D: ELECTRONIC AND MAGNETIC PROPERTIES OF $(\text{LaNiO}_{3-\delta})_1/(\text{LaAlO}_3)_1(001)$ SUPERLATTICES, $\delta = 0.125, 0.25, \text{ AND } 0.5$

1. Stability of different magnetic configurations and distribution of oxygen vacancies at $\delta = 0.125, 0.25, \text{ and } 0.5$

In this section, we assess the stability of different configurations of $(\text{LaNiO}_{3-\delta})_1/(\text{LaAlO}_3)_1(001)$ SLs, $\delta = 0.125, 0.25, \text{ and } 0.5$, respectively. From Table II, we conclude that the single oxygen vacancy has a strong tendency to occupy the

TABLE IV. Stabilization energy [$\Delta E = E$ [S-type AFM order with four oxygen vacancies arranged in configurations (b) or (c) (see Fig. 13)] $- E$ (ground state with S-AFM order with four oxygen vacancies in configuration (a) (see Fig. 13), per Ni atom] of $(\text{LaNiO}_{2.5})_1/(\text{LaAlO}_3)_1(001)$ SL at a_{STO} and a_{LSAO} , respectively.

Configuration and MO	ΔE at a_{STO} (meV per Ni atom)	ΔE at a_{LSAO} (meV per Ni atom)
S-AFM in configuration (b)	118	69
S-AFM in configuration (c)	179	54

NiO_2 plane in $(\text{LaNiO}_{2.875})_1/(\text{LaAlO}_3)_1(001)$ SL, irrespective of strain, as shown in Fig. 12. Further, for $\delta = 0.125$, we compare the total energies of the ground state ferrimagnetic (FiM) order with other possible magnetic configurations in Table III at tensile and compressive strain. Note that albeit the two released electrons are accommodated at two out of eight Ni sites, an overall magnetic moment of 0 μ_{B} /supercell was obtained in both G- and S-AFM orders, respectively, irrespective of strain. For $\delta = 0.25$, all possible initial magnetic configurations result in ferrimagnetic (FiM) order. The ground state FiM order is discussed in Sec. VI above.

Next, we compare the total energies (Table IV) of all possible configurations for Ni^{2+} sites with S-type AFM order in the $(\text{LaNiO}_{2.5})_1/(\text{LaAlO}_3)_1(001)$ SL with four oxygen vacancies shown in Fig. 13 at tensile and compressive strain, respectively. S-type AFM order turns out to be the most favorable magnetic order for all studied oxygen concentrations and the configuration (a) constitutes the ground state. Finally, we comment on the relative stability of different magnetic phases at $\delta = 0.5$. Irrespective of strain, we obtained only stripe AFM and FM magnetic ordering. The S-type AFM order comprises alternating stripes of Ni^{2+} (high-spin) and Ni^{2+} (low-spin) and oxygen vacancies ordered along the $[110]$ direction. Further, the Ni spins couple antiferromagnetically along the Ni^{2+} (high-spin) stripe (discussed in Sec. VI above). The S-FM order is similar to S-AFM except for FM coupling of Ni spins along the Ni^{2+} (high-spin) stripe. The S-AFM magnetic order is more stable than S-FM magnetic order by 31 meV/Ni atom at a_{STO} and 27 meV/Ni atom at a_{LSAO} , respectively.

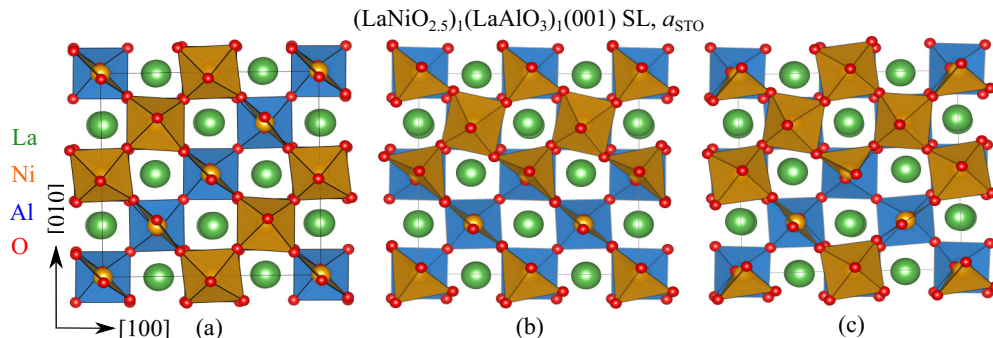


FIG. 13. Top views of the optimized $(\text{LaNiO}_{2.5})_1/(\text{LaAlO}_3)_1(001)$ SLs at a_{STO} with octahedral tilts and rotations for different positions of four basal oxygen vacancies in the NiO_2 plane.

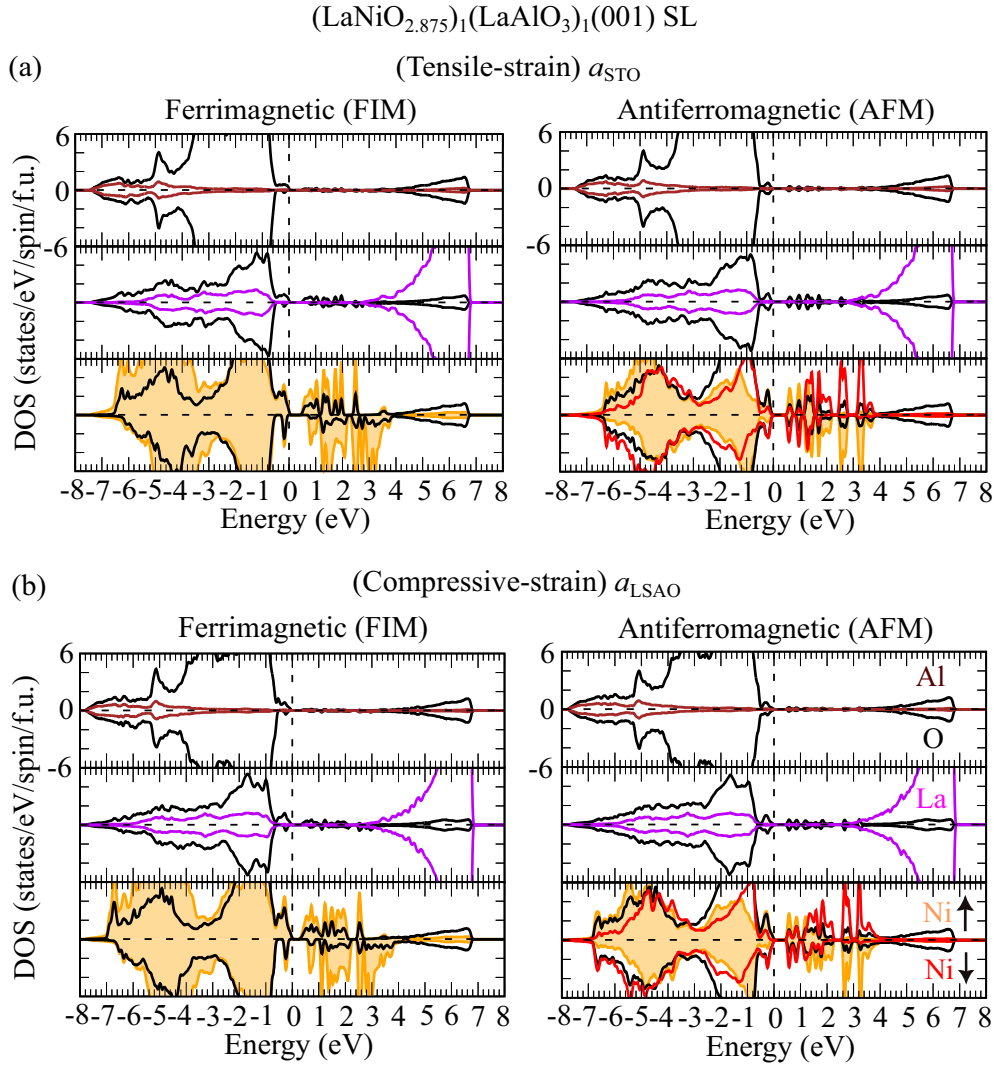


FIG. 14. Layer-, element-, and spin-resolved densities of states for FIM-CD and S-AFM orders in (LaNiO_{2.875})₁/(LaAlO₃)₁(001) SL (a) at a_{STO} (tensile strain) and (b) at a_{LSAO} (compressive strain). In the projected density of states, magenta, black, and brown color represent La, O, and Al states, respectively. Additionally, in FIM cases, filled orange curves represent the Ni states, the PDOS have been averaged over all the corresponding sites in a supercell and normalized to one SL formula unit. In the AFM cases, filled orange and red lines represent Ni sites with positive and negative magnetic moments, respectively. The dashed line at zero energy represents the Fermi level.

2. Localization of excess electrons in the (LaNiO_{2.875})₁/(LaAlO₃)₁(001) superlattices

Besides the S-stripe FIM phase, we modeled S-type AFM ordering of Ni spins in (LaNiO_{2.875})₁/(LaAlO₃)₁(001) SL at tensile and compressive strain, respectively. S-type AFM order is characterized by a stripe like arrangement of ferro/antiferromagnetic Ni spins along the $[\bar{1}10]$ direction. In S-type AFM order at $\delta = 0.125$, the two released electrons are accommodated at the Ni6 [$1.55 \mu_B$ (a_{STO})/ $1.46 \mu_B$ (a_{LSAO})] and Ni7 [$1.54 \mu_B$ (a_{STO})/ $1.46 \mu_B$ (a_{LSAO})] sites, respectively [marked in Fig. 15(a)], with zero total magnetization of the supercell. This is different from the FIM-CD phase leading to a net magnetic moment of $\sim 6 \mu_B$ /supercell, irrespective of strain. Figure 14 shows the comparison of layer-, element-, and spin-resolved densities of states for FIM-CD and S-AFM and order in (LaNiO_{2.875})₁/(LaAlO₃)₁(001) SL at tensile and

compressive strain, respectively. Despite the opening of a band gap for both magnetic configurations, we found that the FIM-CD phase is more stable than the S-AFM phase by 26 and 27.5 meV per Ni ion at a_{STO} and a_{LSAO} , respectively. This clearly indicates the electron localization as the preferred mechanism for MIT in (LaNiO_{3- δ)₁/(LaAlO₃)₁(001) SLs.}

3. Electronic properties of (LaNiO_{3- δ)₁/(LaAlO₃)₁(001) superlattices, $\delta = 0.125, 0.25$, and 0.5}

The orbital projected DOS of the Ni sites with distinct spin moments and symmetry inequivalence in (LaNiO_{3- δ)₁/(LaAlO₃)₁(001) SLs ($\delta = 0.125$ and 0.25) along with the density of states of the apical and basal oxygen associated with their polyhedra are shown in Fig. 15 ($\delta = 0.125$) and Fig. 16 ($\delta = 0.25$), for both tensile and}

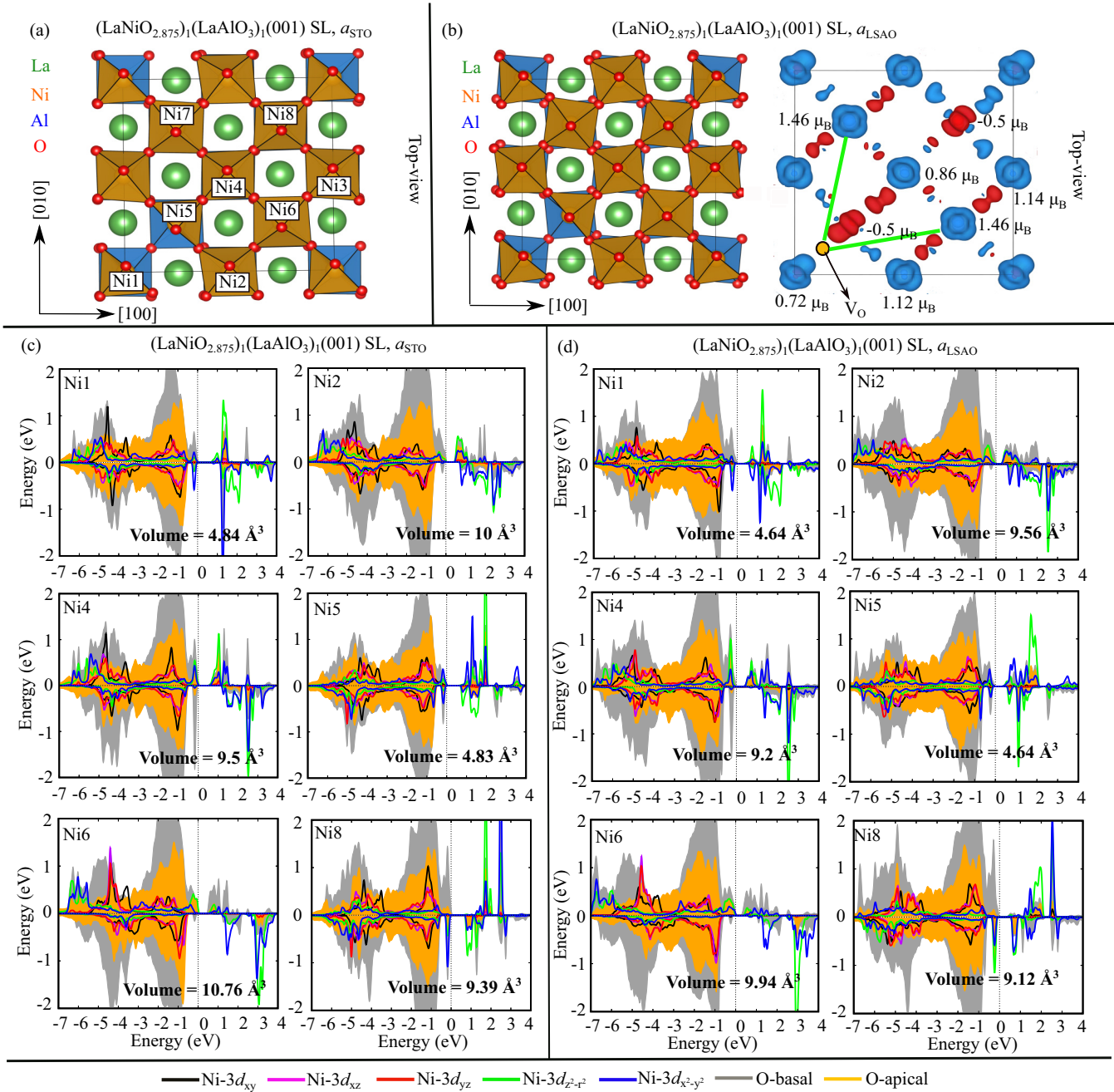


FIG. 15. (a) Top view of the optimized $(\text{LaNiO}_{2.875})_1/(\text{LaAlO}_3)_1(001)$ SL at a_{STO} . All Ni sites with distinct spin moments are marked. (b) Top view of the optimized structure of $(\text{LaNiO}_{2.875})_1/(\text{LaAlO}_3)_1(001)$ SL at a_{LSAO} and the corresponding spin-density plot. Blue and red colors denote positive and negative spin densities, respectively. Spin densities are integrated between -7 eV up to the Fermi level. Arrows mark the oxygen vacancy sites and the localization sites for the released electrons with respect to the oxygen vacancy sites are connected with green lines. The isovalue of the spin density is $0.006 \text{ e}/\text{\AA}^3$. Orbital projected density of states of the Ni sites in $(\text{LaNiO}_{2.875})_1/(\text{LaAlO}_3)_1(001)$ SL having distinct spin moments and symmetry inequivalence together with the density of states of the apical and basal oxygen associated with the corresponding polyhedra at (c) a_{STO} and (d) a_{LSAO} , respectively.

compressive strain, respectively. Similarly, at $\delta = 0.5$, the orbital projected density of states of the Ni^{2+} (low spin) and Ni^{2+} (high spin) along with the density of states of the apical and basal oxygen associated with the NiO_4 square planar plaquettes and the NiO_6 octahedra, respectively, are shown in Fig. 17(c), at compressive strain. Figures 18 and 19 show the electronic band structure diagrams and the layer-resolved

density of states (LDOS) at tensile and compressive strains, respectively. In all the cases, the Ni $3d$ states lie in the band gap of LaAlO_3 , while La $4f$ states remain between ~ 4 to 7 eV, irrespective of strain. The electronic properties in the vicinity of the Fermi level are governed mainly by the Ni $3d$ states admixed with O $2p$ states, with negligible contributions from La and Al states, irrespective of strain.

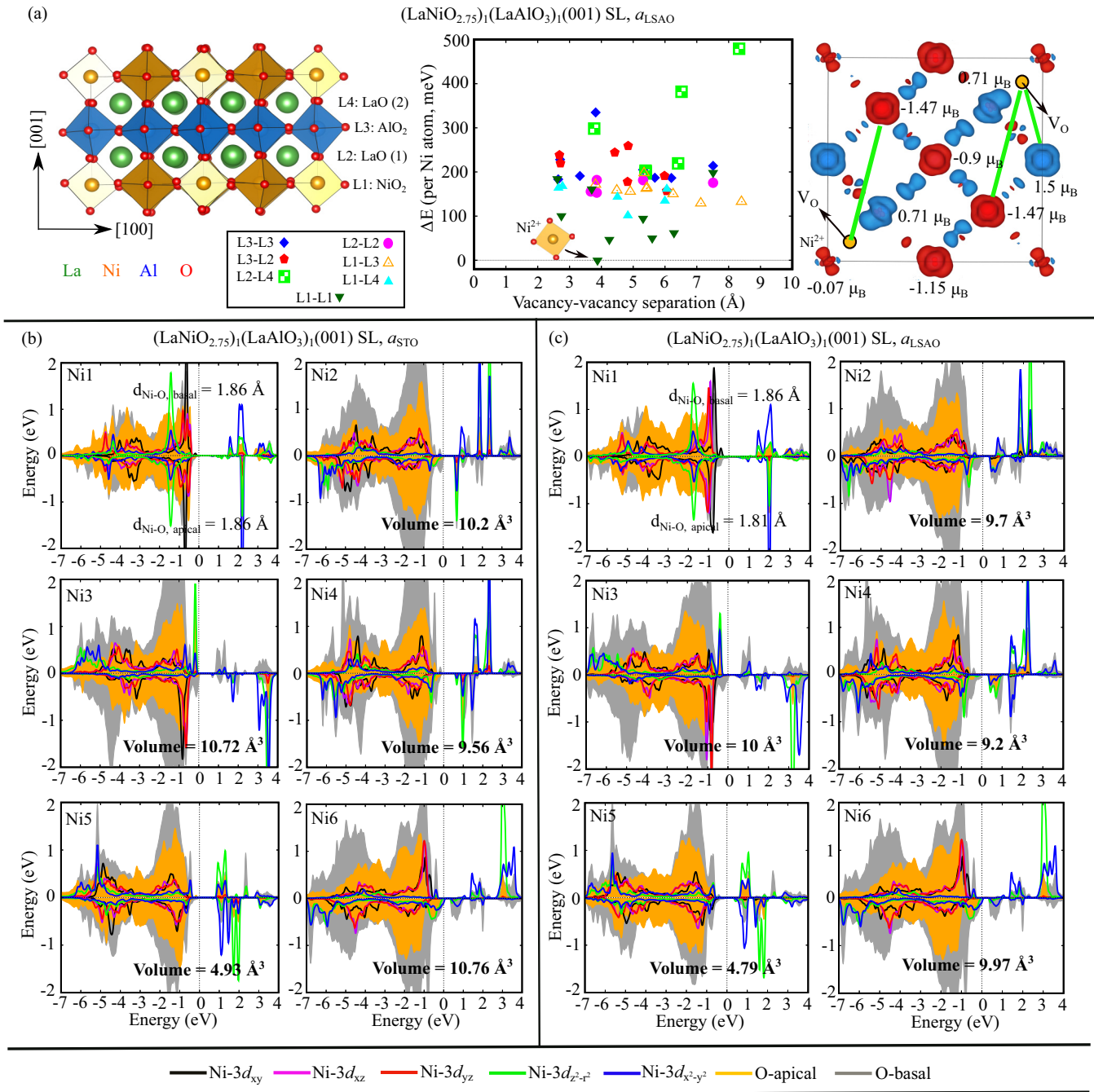


FIG. 16. (a) Side view of the optimized structure of $(\text{LaNiO}_{2.75})_1/(\text{LaAlO}_3)_1(001)$ SL at a_{LSAO} (compressive strain). L1 to L4 denote the planes in the SL. L_i-L_j indicates in which layer the two vacancies are located. Relative energy difference of all possible configurations for two oxygen vacancies in a $(\text{LaNiO}_{2.75})_1/(\text{LaAlO}_3)_1(001)$ SL at a_{LSAO} . ΔE with respect to the most stable configuration as a function of the distance between the vacancies. The spin-density of the lowest energy case with Ni^{2+} (LS) site in a fourfold coordination at a_{LSAO} is displayed on the right. Blue and red colors denote positive and negative spin densities, respectively. Spin densities are integrated between -7 eV up to the Fermi level. The isovalue of the spin density is $0.006 \text{ e}/\text{\AA}^3$. The oxygen vacancy sites and the localization sites for the released electrons are connected with green lines. Orbital projected density of states of the Ni sites in $(\text{LaNiO}_{2.75})_1/(\text{LaAlO}_3)_1(001)$ SL having distinct spin moments and symmetry inequivalence along with the density of states of the apical and basal oxygen associated with their corresponding polyhedra (b) a_{STO} (tensile strain), and (c) a_{LSAO} (compressive strain), respectively.

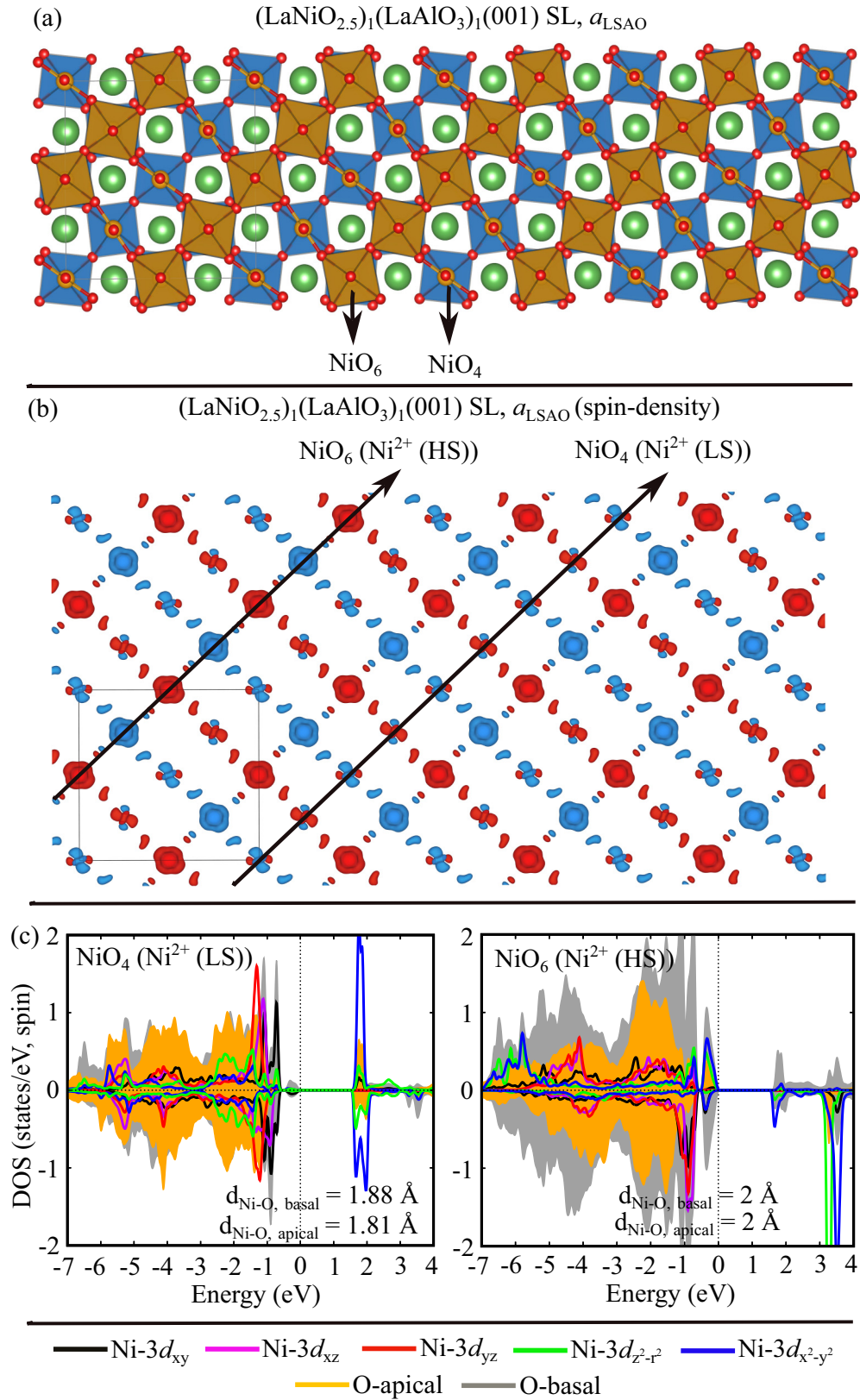


FIG. 17. (a) Top view of the optimized $(\text{LaNiO}_{2.5})_1/(\text{LaAlO}_3)_1(001)$ SL at a_{LSAO} . (b) Spin density integrated between -7 eV up to the Fermi level. The isovalue of the spin-density is $0.006 \text{ e}/\text{\AA}^3$. Blue and red colors correspond to positive and negative spin densities, respectively. (c) The orbital projected density of states of the Ni^{2+} (low spin), left and Ni^{2+} (high spin), right, respectively, along with the density of states of the apical and basal oxygen associated with the NiO_4 square planar plaquettes (left) and the NiO_6 octahedra (right).

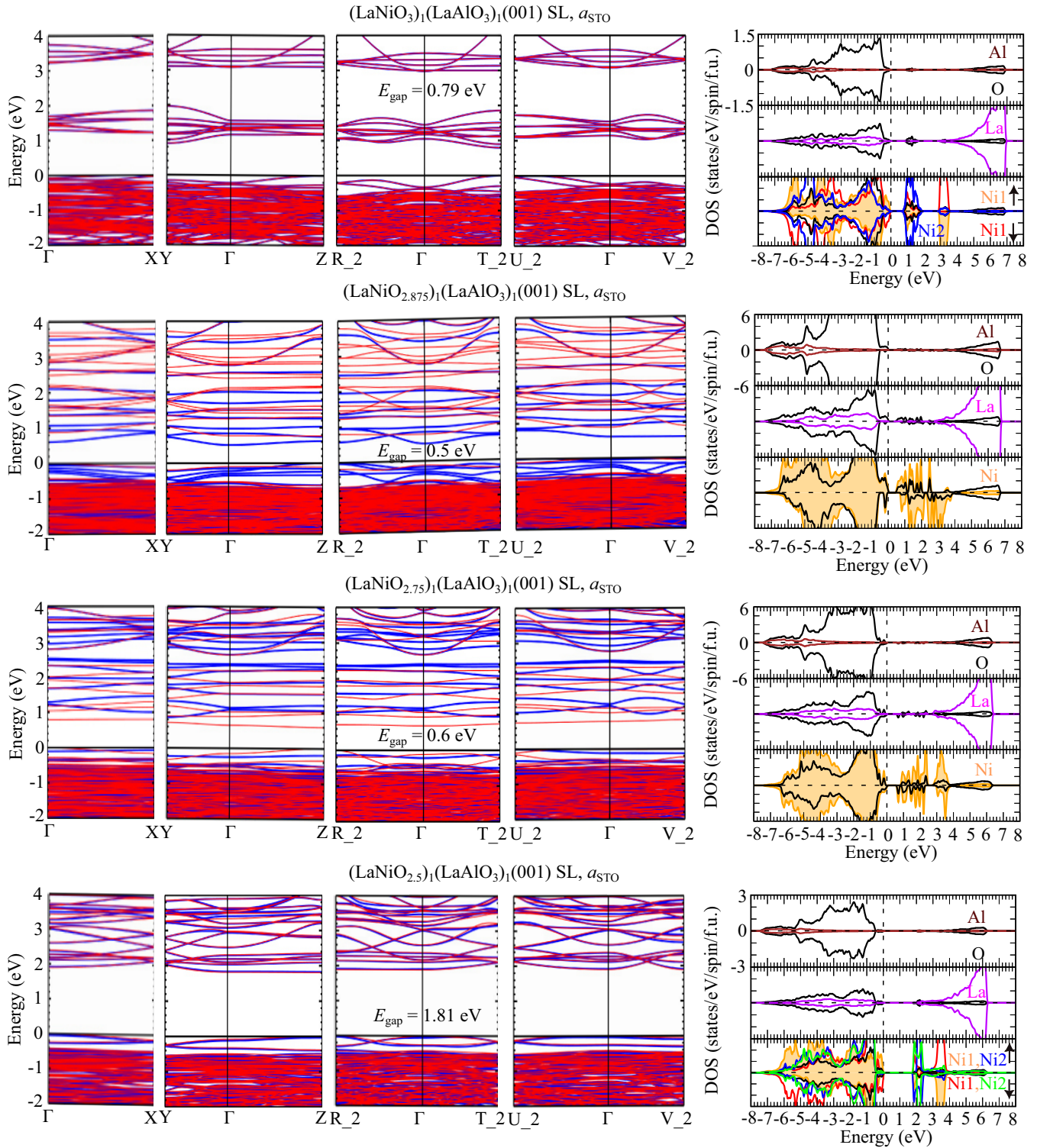


FIG. 18. Electronic band structure and the corresponding layer-, element-, and spin-resolved densities of states for $(\text{LaNiO}_{3-\delta})_1/(\text{LaAlO}_3)_1(001)$ SLs at a_{STO} (tensile strain). Blue and red represent majority and minority bands in the band structure, respectively. In the projected density of states, magenta, black, and brown color represent La, O, and Al states, respectively. Additionally, in the NiO_2 panel of the pristine SL case, orange areas and red lines denote the PDOS of the Ni1 $[(d^8)_{S=1}]$ sites with positive and negative magnetic moments, whereas blue lines represents the PDOS of the Ni2 $[(d^8L^2)_{S=0}]$ sites. For $\delta = 0.125$ and 0.25 , filled orange areas represent the Ni states and the PDOS have been averaged over all the corresponding sites in a supercell and normalized to one SL formula unit. Finally for $\delta = 0.5$, filled orange areas and red lines represent the Ni1 [high-spin (HS)] sites with positive and negative magnetic moments, whereas blue and green lines represent the Ni2 [low-spin (LS)] sites with nearly zero magnetic moment, respectively. The dashed vertical line at zero energy represents the Fermi level.

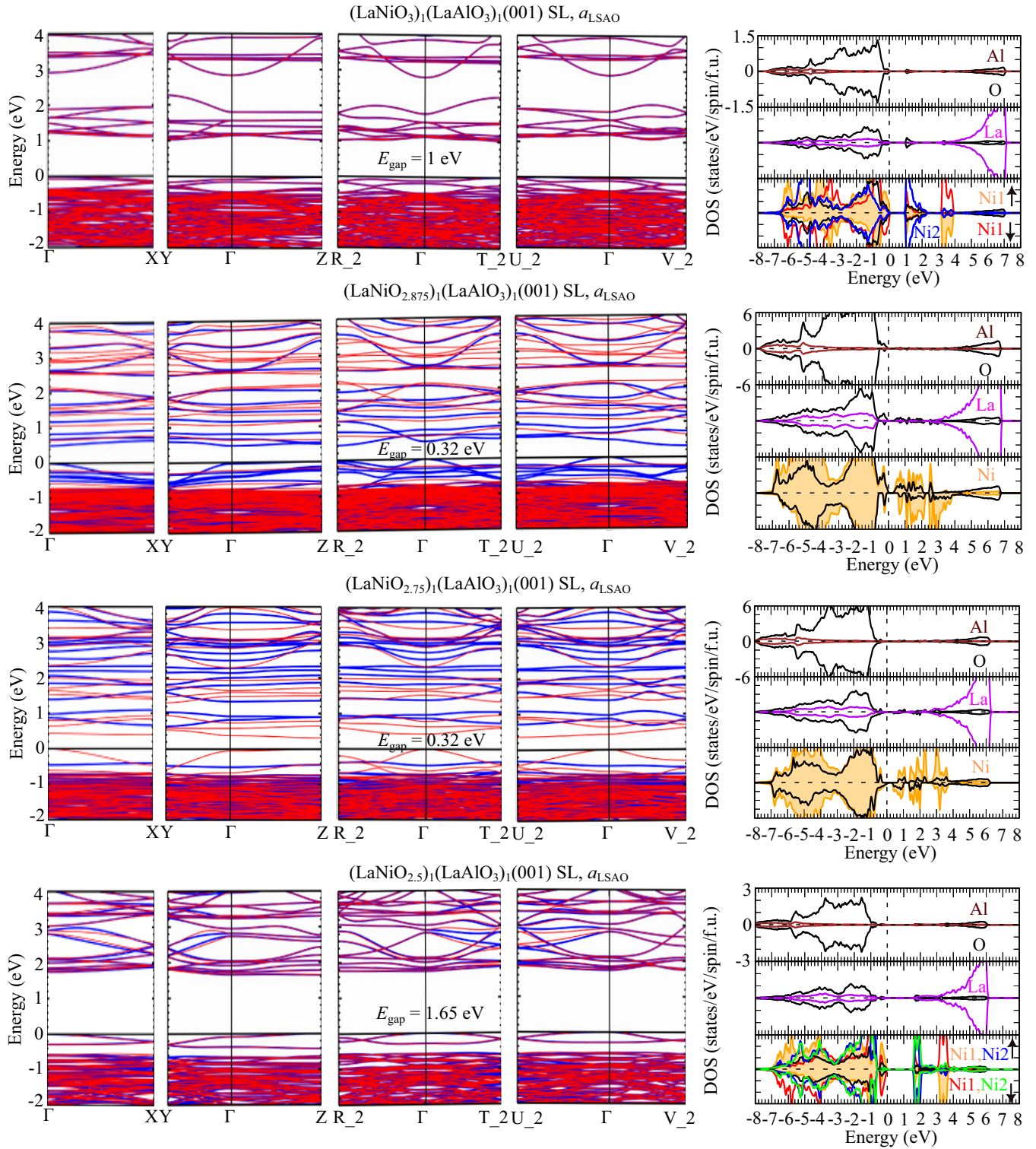


FIG. 19. Electronic band structure (blue/red correspond to majority/minority bands, respectively) and the corresponding layer-, element-, and spin-resolved densities of states for $(\text{LaNiO}_{3-\delta})_1/(\text{LaAlO}_3)_1(001)$ SLs at a_{LSAO} (compressive strain). In the projected density of states, magenta, black, and brown color represent La, O, and Al states, respectively. Additionally, in the NiO_2 panel of the pristine SL case, filled orange area and red lines represent the Ni1 ($(d^8)_{S=1}$) sites with positive and negative magnetic moments, whereas, blue line represents the PDOS of the Ni2 ($(d^8L^2)_{S=0}$) site. For $\delta = 0.125$ and 0.25 , filled orange areas represent the Ni states and the PDOS have been averaged over all the corresponding sites in a supercell and normalized to one SL formula unit. Finally for the $\delta = 0.5$ case, filled orange areas and red lines represent the Ni1 [high-spin (HS)] sites with positive and negative magnetic moments, whereas, blue and green lines represent the Ni2 [low-spin (LS)] sites with nearly zero magnetic moment, respectively. The dashed line at zero energy represents the Fermi level.

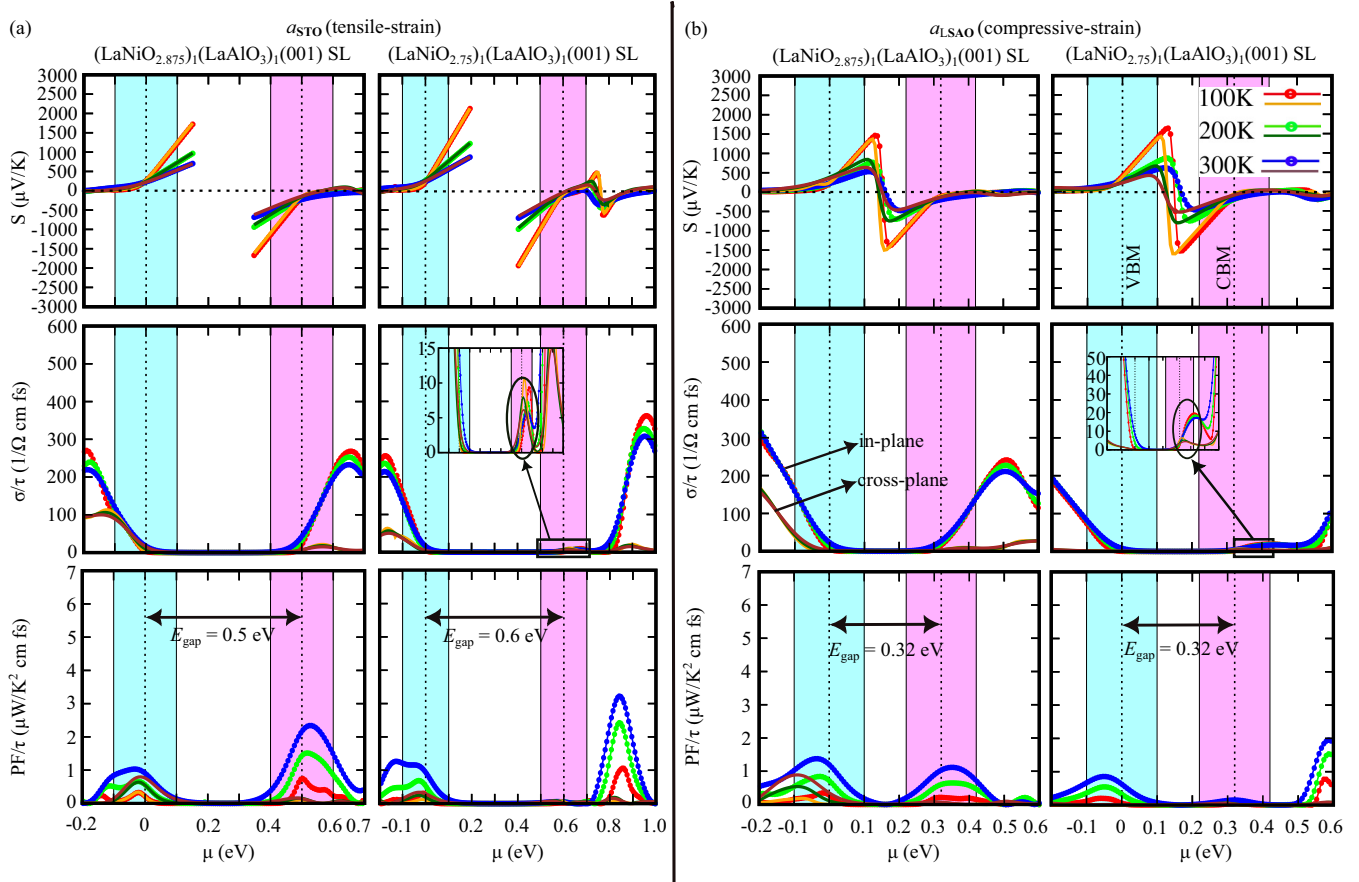


FIG. 20. Thermoelectric properties of $(\text{LaNiO}_{3-\delta})_1/(\text{LaAlO}_3)_1(001)$ SL ($\delta = 0.125$ and 0.25) at (a) a_{STO} and (b) a_{LSAO} , for three different temperatures 100, 200, and 300. From top to bottom, Seebeck coefficient S , electrical conductivity σ/τ , and the electronic power factor PF/τ are shown, where τ denotes the relaxation time. Orange, dark-green, and brown lines (red, green, and blue dotted lines) correspond to cross-plane (in-plane) transport. The vertical dashed line at zero energy denotes the Fermi level and the VBM; in the latter case, the second vertical dashed line indicates the CBM. The energy window of physical importance (± 100 meV around the band edges) are marked in cyan (at VBM) and magenta (at CBM), respectively.

APPENDIX E: THERMOELECTRIC PROPERTIES OF $(\text{LaNiO}_{3-\delta})_1/(\text{LaAlO}_3)_1(001)$ SUPERLATTICES, $\delta = 0.125$ AND 0.25

Figure 20 shows the thermoelectric properties of $(\text{LaNiO}_{3-\delta})_1/(\text{LaAlO}_3)_1(001)$ SLs for $\delta = 0.125$ and 0.25 , at tensile and compressive strain.

- [1] P. Zubko, S. Gariglio, M. Gabay, P. Ghosez, and J.-M. Triscone, Interface physics in complex oxide heterostructures, *Annu. Rev. Condens. Matter Phys.* **2**, 141 (2011).
- [2] M. Lorenz, M. S. R. Rao, T. Venkatesan, E. Fortunato, P. Barquinha, R. Branquinho, D. Salgueiro, R. Martins, E. Carlos, A. Liu, F. K. Shan, M. Grundmann, H. Boschker, J. Mukherjee, M. Priyadarshini, N. DasGupta, D. J. Rogers, F. H. Teherani, E. V. Sandana, P. Bove, K. Rietwyk, A. Zaban, A. Veziridis, A. Weidenkaff, M. Muralidhar, M. Murakami, S. Abel, J. Fompeyrine, J. Zuniga-Perez, R. Ramesh, N. A. Spaldin, S. Ostanin, V. Borisov, I. Mertig, V. Lazenka, G. Srinivasan, W. Prellier, M. Uchida, M. Kawasaki, R. Pentcheva, P. Gegenwart, F. M. Granozio, J. Fontcuberta, and N. Pryds, The 2016 oxide electronic materials and oxide interfaces roadmap, *J. Phys. D* **49**, 433001 (2016).
- [3] R. Ramesh and D. G. Schlom, Creating emergent phenomena in oxide superlattices, *Nat. Rev. Mater.* **4**, 257 (2019).
- [4] J. Mannhart and D. G. Schlom, Oxide interfaces—an opportunity for electronics, *Science* **327**, 1607 (2010).
- [5] Z. Ali, Z. Wang, A. O'Hara, M. Saghayezhian, D. Shin, Y. Zhu, S. T. Pantelides, and J. Zhang, Origin of insulating and non-ferromagnetic SrRuO_3 monolayers, *Phys. Rev. B* **105**, 054429 (2022).
- [6] M. L. Medarde, Structural, magnetic and electronic properties of perovskites $R = \text{rare earth}$, *J. Phys.: Condens. Matter* **9**, 1679 (1997).
- [7] T. Mizokawa, D. I. Khomskii, and G. A. Sawatzky, Spin and charge ordering in self-doped mott insulators, *Phys. Rev. B* **61**, 11263 (2000).

- [8] H. Park, A. J. Millis, and C. A. Marianetti, Site-selective mott transition in rare-earth-element nickelates, *Phys. Rev. Lett.* **109**, 156402 (2012).
- [9] B. Lau and A. J. Millis, Theory of the magnetic and metal-insulator transitions in $R\text{NiO}_3$ bulk and layered structures, *Phys. Rev. Lett.* **110**, 126404 (2013).
- [10] T. Mizokawa, A. Fujimori, T. Arima, Y. Tokura, N. Mori, and J. Akimitsu, Electronic structure of PrNiO_3 studied by photoemission and x-ray-absorption spectroscopy: Band gap and orbital ordering, *Phys. Rev. B* **52**, 13865 (1995).
- [11] Y. Bodenthin, U. Staub, C. Piamonteze, M. García-Fernández, M. J. Martínez-Lope, and J. A. Alonso, Magnetic and electronic properties of $R\text{NiO}_3$, $R = \text{Pr, Nd, Eu, Ho}$ and Y perovskites studied by resonant soft x-ray magnetic powder diffraction, *J. Phys.: Condens. Matter* **23**, 036002 (2011).
- [12] M. Abbate, G. Zampieri, F. Prado, A. Caneiro, J. M. Gonzalez-Calbet, and M. Vallet-Regí, Electronic structure and metal-insulator transition in $\text{LaNiO}_{3-\delta}$, *Phys. Rev. B* **65**, 155101 (2002).
- [13] K. Horiba, R. Eguchi, M. Taguchi, A. Chainani, A. Kikkawa, Y. Senba, H. Ohashi, and S. Shin, Electronic structure of LaNiO_{3-x} : An in situ soft x-ray photoemission and absorption study, *Phys. Rev. B* **76**, 155104 (2007).
- [14] M. J. Han and M. van Veenendaal, Spin-moment formation and reduced orbital polarization in $\text{LaNiO}_3/\text{LaAlO}_3$ superlattice: LDA + U study, *Phys. Rev. B* **85**, 195102 (2012).
- [15] V. I. Anisimov, D. Bukhvalov, and T. M. Rice, Electronic structure of possible nickelate analogs to the cuprates, *Phys. Rev. B* **59**, 7901 (1999).
- [16] R. J. Green, M. W. Haverkort, and G. A. Sawatzky, Bond disproportionation and dynamical charge fluctuations in the perovskite rare-earth nickelates, *Phys. Rev. B* **94**, 195127 (2016).
- [17] S. Johnston, A. Mukherjee, I. Elfimov, M. Berciu, and G. A. Sawatzky, Charge disproportionation without charge transfer in the rare-earth-element nickelates as a possible mechanism for the metal-insulator transition, *Phys. Rev. Lett.* **112**, 106404 (2014).
- [18] V. Bisogni, S. Catalano, R. J. Green, M. Gibert, R. Scherwitzl, Y. Huang, V. N. Strocov, P. Zubko, S. Balandeh, J.-M. Triscone, G. Sawatzky, and T. Schmitt, Ground-state oxygen holes and the metal-insulator transition in the negative charge-transfer rare-earth nickelates, *Nat. Commun.* **7**, 13017 (2016).
- [19] J. B. Torrance, P. Lacorre, A. I. Nazzari, E. J. Ansaldo, and C. Niedermayer, Systematic study of insulator-metal transitions in perovskites $R\text{NiO}_3$ $R=\text{Pr, Nd, Sm, Eu}$ due to closing of charge-transfer gap, *Phys. Rev. B* **45**, 8209 (1992).
- [20] I. I. Mazin, D. I. Khomskii, R. Lengsdorf, J. A. Alonso, W. G. Marshall, R. M. Ibberson, A. Podlesnyak, M. J. Martínez-Lope, and M. M. Abd-Elmeguid, Charge ordering as alternative to jahn-teller distortion, *Phys. Rev. Lett.* **98**, 176406 (2007).
- [21] J. W. Freeland, J. Liu, M. Kareev, B. Gray, J. W. Kim, P. Ryan, R. Pentcheva, and J. Chakhalian, Orbital control in strained ultra-thin $\text{LaNiO}_3/\text{LaAlO}_3$ superlattices, *Europhys. Lett.* **96**, 57004 (2011).
- [22] A. Blanca-Romero and R. Pentcheva, Confinement-induced metal-to-insulator transition in strained $\text{LaNiO}_3/\text{LaAlO}_3$ superlattices, *Phys. Rev. B* **84**, 195450 (2011).
- [23] B. Geisler and R. Pentcheva, Confinement- and strain-induced enhancement of thermoelectric properties in $\text{LaNiO}_3/\text{LaAlO}_3(001)$ superlattices, *Phys. Rev. Mater.* **2**, 055403 (2018).
- [24] R. Scherwitzl, P. Zubko, C. Lichtensteiger, and J.-M. Triscone, Electric-field tuning of the metal-insulator transition in ultrathin films of LaNiO_3 , *Appl. Phys. Lett.* **95**, 222114 (2009).
- [25] P. D. C. King, H. I. Wei, Y. F. Nie, M. Uchida, C. Adamo, S. Zhu, X. He, I. Božović, D. G. Schlom, and K. M. Shen, Atomic-scale control of competing electronic phases in ultrathin LaNiO_3 , *Nat. Nanotechnol.* **9**, 443 (2014).
- [26] D. P. Kumah, A. Malashevich, A. S. Disa, D. A. Arena, F. J. Walker, S. Ismail-Beigi, and C. H. Ahn, Effect of surface termination on the electronic properties of LaNiO_3 films, *Phys. Rev. Applied* **2**, 054004 (2014).
- [27] M. Gabay and J.-M. Triscone, It takes two to waver, *Nat. Nanotechnol.* **9**, 417 (2014).
- [28] J. Son, P. Moetakef, J. M. LeBeau, D. Ouellette, L. Balents, S. J. Allen, and S. Stemmer, Low-dimensional mott material: Transport in ultrathin epitaxial LaNiO_3 films, *Appl. Phys. Lett.* **96**, 062114 (2010).
- [29] R. Scherwitzl, S. Gariglio, M. Gabay, P. Zubko, M. Gibert, and J.-M. Triscone, Metal-insulator transition in ultrathin LaNiO_3 films, *Phys. Rev. Lett.* **106**, 246403 (2011).
- [30] E. Sakai, M. Tamamitsu, K. Yoshimatsu, S. Okamoto, K. Horiba, M. Oshima, and H. Kumigashira, Gradual localization of $\text{Ni } 3d$ states in LaNiO_3 ultrathin films induced by dimensional crossover, *Phys. Rev. B* **87**, 075132 (2013).
- [31] J. Liu, S. Okamoto, M. van Veenendaal, M. Kareev, B. Gray, P. Ryan, J. W. Freeland, and J. Chakhalian, Quantum confinement of mott electrons in ultrathin $\text{LaNiO}_3/\text{LaAlO}_3$ superlattices, *Phys. Rev. B* **83**, 161102(R) (2011).
- [32] A. V. Boris, Y. Matiks, E. Benckiser, A. Frano, P. Popovich, V. Hinkov, P. Wochner, M. Castro-Colin, E. Detemple, V. K. Malik, C. Bernhard, T. Prokscha, A. Suter, Z. Salman, E. Morenzoni, G. Cristiani, H.-U. Habermeier, and B. Keimer, Dimensionality control of electronic phase transitions in nickel-oxide superlattices, *Science* **332**, 937 (2011).
- [33] S. Middey, D. Meyers, M. Kareev, Y. Cao, X. Liu, P. Shafer, J. W. Freeland, J.-W. Kim, P. J. Ryan, and J. Chakhalian, Disentangled cooperative orderings in artificial rare-earth nickelates, *Phys. Rev. Lett.* **120**, 156801 (2018).
- [34] D. Puggioni, A. Filippetti, and V. Fiorentini, Ordering and multiple phase transitions in ultrathin nickelate superlattices, *Phys. Rev. B* **86**, 195132 (2012).
- [35] A. Filippetti and V. Fiorentini, A practical first-principles band-theory approach to the study of correlated materials, *Eur. Phys. J. B* **71**, 139 (2009).
- [36] T. Archer, C. D. Pemmaraju, S. Sanvito, C. Franchini, J. He, A. Filippetti, P. Delugas, D. Puggioni, V. Fiorentini, R. Tiwari, and P. Majumdar, Exchange interactions and magnetic phases of transition metal oxides: Benchmarking advanced ab initio methods, *Phys. Rev. B* **84**, 115114 (2011).
- [37] B.-X. Wang, S. Rosenkranz, X. Rui, J. Zhang, F. Ye, H. Zheng, R. F. Klie, J. F. Mitchell, and D. Phelan, Antiferromagnetic defect structure in $\text{LaNiO}_{3\delta}$ single crystals, *Phys. Rev. Mater.* **2**, 064404 (2018).
- [38] K. Dey, W. Herggett, P. Telang, M. M. Abdel-Hafiez, and R. Klingeler, Magnetic properties of high-pressure optical floating-zone grown LaNiO_3 single crystals, *J. Cryst. Growth* **524**, 125157 (2019).

- [39] H. Guo, Z. W. Li, L. Zhao, Z. Hu, C. F. Chang, C.-Y. Kuo, W. Schmidt, A. Piovano, T. W. Pi, O. Sobolev, D. I. Khomskii, L. H. Tjeng, and A. C. Komarek, Antiferromagnetic correlations in the metallic strongly correlated transition metal oxide LaNiO_3 , *Nat. Commun.* **9**, 43 (2018).
- [40] C. Liu, V. F. C. Humbert, T. M. Bretz-Sullivan, G. Wang, D. Hong, F. Wrobel, J. Zhang, J. D. Hoffman, J. E. Pearson, J. S. Jiang, C. Chang, A. Suslov, N. Mason, M. R. Norman, and A. Bhattacharya, Observation of an antiferromagnetic quantum critical point in high-purity LaNiO_3 , *Nat. Commun.* **11**, 1402 (2020).
- [41] X. Liao, V. Singh, and H. Park, Oxygen vacancy induced site-selective mott transition in LaNiO_3 , *Phys. Rev. B* **103**, 085110 (2021).
- [42] M. Kawai, S. Inoue, M. Mizumaki, N. Kawamura, N. Ichikawa, and Y. Shimakawa, Reversible changes of epitaxial thin films from perovskite LaNiO_3 to infinite-layer structure LaNiO_2 , *Appl. Phys. Lett.* **94**, 082102 (2009).
- [43] I-Cheng Tung, G. Luo, J. H. Lee, S. H. Chang, J. Moyer, H. Hong, M. J. Bedzyk, H. Zhou, D. Morgan, D. D. Fong, and J. W. Freeland, Polarity-driven oxygen vacancy formation in ultrathin LaNiO_3 films on SrTiO_3 , *Phys. Rev. Mater.* **1**, 053404 (2017).
- [44] M. Kotiuga, Z. Zhang, J. Li, F. Rodolakis, H. Zhou, R. Sutarto, F. He, Q. Wang, Y. Sun, Y. Wang, N. A. Aghamiri, S. B. Hancock, L. P. Rokhinson, D. P. Landau, Y. Abate, J. W. Freeland, R. Comin, S. Ramanathan, and K. M. Rabe, Carrier localization in perovskite nickelates from oxygen vacancies, *Proc. Natl. Acad. Sci. USA* **116**, 21992 (2019).
- [45] M. Kotiuga and K. M. Rabe, High-density electron doping of SmNiO_3 from first principles, *Phys. Rev. Mater.* **3**, 115002 (2019).
- [46] Y. Shin and J. M. Rondinelli, Magnetic structure of oxygen-deficient perovskite nickelates with ordered vacancies, *Phys. Rev. Res.* **4**, L022069 (2022).
- [47] A. Malashevich and S. Ismail-Beigi, First-principles study of oxygen-deficient LaNiO_3 structures, *Phys. Rev. B* **92**, 144102 (2015).
- [48] J. Liu, M. Kareev, S. Prosandeev, B. Gray, P. Ryan, J. W. Freeland, and J. Chakhalian, Effect of polar discontinuity on the growth of $\text{LaNiO}_3/\text{LaAlO}_3$ superlattices, *Appl. Phys. Lett.* **96**, 133111 (2010).
- [49] B. Geisler, S. Follmann, and R. Pentcheva, Oxygen vacancy formation and electronic reconstruction in strained LaNiO_3 and $\text{LaNiO}_3/\text{LaAlO}_3$ superlattices, *Phys. Rev. B* **106**, 155139 (2022).
- [50] C. Yu, M. L. Scullin, M. Huijben, R. Ramesh, and A. Majumdar, Thermal conductivity reduction in oxygen-deficient strontium titanates, *Appl. Phys. Lett.* **92**, 191911 (2008).
- [51] M. Verma and R. Pentcheva, Metal-insulator transition and robust thermoelectricity via strain-tuned interplay between structural and electronic properties in $(\text{SrVO}_3)_1/(\text{SrTiO}_3)_1(001)$ superlattices, *Phys. Rev. Res.* **4**, 033013 (2022).
- [52] B. Jalan and S. Stemmer, Large seebeck coefficients and thermoelectric power factor of La-doped SrTiO_3 thin films, *Appl. Phys. Lett.* **97**, 042106 (2010).
- [53] T. Okuda, K. Nakanishi, S. Miyasaka, and Y. Tokura, Large thermoelectric response of metallic perovskites: $\text{Sr}_{1-x}\text{La}_x\text{TiO}_3$ ($0 < x < \sim 0.1$), *Phys. Rev. B* **63**, 113104 (2001).
- [54] S. Ohta, T. Nomura, H. Ohta, and K. Koumoto, High-temperature carrier transport and thermoelectric properties of heavily La- or Nb-doped SrTiO_3 single crystals, *J. Appl. Phys.* **97**, 034106 (2005).
- [55] M. Verma, B. Geisler, and R. Pentcheva, Effect of confinement and octahedral rotations on the electronic, magnetic, and thermoelectric properties of correlated $\text{SrXO}_3/\text{SrTiO}_3(001)$ superlattices ($X = \text{V}, \text{Cr}, \text{or Mn}$), *Phys. Rev. B* **100**, 165126 (2019).
- [56] W. Kohn and L. J. Sham, Self-consistent equations including exchange and correlation effects, *Phys. Rev.* **140**, A1133 (1965).
- [57] G. Kresse and J. Hafner, Ab initio molecular dynamics for liquid metals, *Phys. Rev. B* **47**, 558 (1993).
- [58] G. Kresse and J. Furthmüller, Efficient iterative schemes for ab initio total-energy calculations using a plane-wave basis set, *Phys. Rev. B* **54**, 11169 (1996).
- [59] P. E. Blöchl, Projector augmented-wave method, *Phys. Rev. B* **50**, 17953 (1994).
- [60] G. Kresse and D. Joubert, From ultrasoft pseudopotentials to the projector augmented-wave method, *Phys. Rev. B* **59**, 1758 (1999).
- [61] J. P. Perdew, K. Burke, and M. Ernzerhof, Generalized gradient approximation made simple, *Phys. Rev. Lett.* **77**, 3865 (1996).
- [62] V. I. Anisimov, I. V. Solovyev, M. A. Korotin, M. T. Czyżyk, and G. A. Sawatzky, Density-functional theory and nio photoemission spectra, *Phys. Rev. B* **48**, 16929 (1993).
- [63] S. L. Dudarev, G. A. Botton, S. Y. Savrasov, C. J. Humphreys, and A. P. Sutton, Electron-energy-loss spectra and the structural stability of nickel oxide: An LSDA+U study, *Phys. Rev. B* **57**, 1505 (1998).
- [64] H. J. Monkhorst and J. D. Pack, Special points for brillouin-zone integrations, *Phys. Rev. B* **13**, 5188 (1976).
- [65] J. L. García-Muñoz, J. Rodríguez-Carvajal, P. Lacorre, and J. B. Torrance, Neutron-diffraction study of $R\text{NiO}_3$ ($R=\text{La}, \text{Pr}, \text{Nd}, \text{Sm}$): Electronically induced structural changes across the metal-insulator transition, *Phys. Rev. B* **46**, 4414 (1992).
- [66] A. Togo, L. Chaput, T. Tadano, and I. Tanaka, Implementation strategies in phonopy and phono3py, *J. Phys.: Condens. Matter* **35**, 353001 (2023).
- [67] A. Togo, First-principles phonon calculations with phonopy and phono3py, *J. Phys. Soc. Jpn.* **92**, 012001 (2023).
- [68] A. M. Ganose, A. J. Jackson, and D. O. Scanlon, sumo: Command-line tools for plotting and analysis of periodic ab initio calculations, *J. Open Source Softw.* **3**, 717 (2018).
- [69] G. K. Madsen and D. J. Singh, Boltztrap: a code for calculating band-structure dependent quantities, *Comput. Phys. Commun.* **175**, 67 (2006).
- [70] U. Sivan and Y. Imry, Multichannel landauer formula for thermoelectric transport with application to thermopower near the mobility edge, *Phys. Rev. B* **33**, 551 (1986).
- [71] B. Geisler, A. Blanca-Romero, and R. Pentcheva, Design of n - and p -type oxide thermoelectrics in $\text{LaNiO}_3/\text{SrTiO}_3(001)$ superlattices exploiting interface polarity, *Phys. Rev. B* **95**, 125301 (2017).
- [72] B. Geisler and R. Pentcheva, Inducing n - and p -type thermoelectricity in oxide superlattices by strain tuning of orbital-selective transport resonances, *Phys. Rev. Appl.* **11**, 044047 (2019).
- [73] V. A. Stoica, D. Puggioni, J. Zhang, R. Singla, G. L. Dakovski, G. Coslovich, M. H. Seaberg, M. Kareev, S. Middey,

- P. Kissin, R. D. Averitt, J. Chakhalian, H. Wen, J. M. Rondinelli, and J. W. Freeland, Magnetic order driven ultrafast phase transition in NdNiO₃, [Phys. Rev. B **106**, 165104 \(2022\)](#).
- [74] D. I. Bilc, C. G. Floare, L. P. Zárbo, S. Garabagiu, S. Lemal, and P. Ghosez, First-principles modeling of SrTiO₃ based oxides for thermoelectric applications, [J. Phys. Chem. C **120**, 25678 \(2016\)](#).
- [75] G. Xing, J. Sun, Y. Li, X. Fan, W. Zheng, and D. J. Singh, Electronic fitness function for screening semiconductors as thermoelectric materials, [Phys. Rev. Mater. **1**, 065405 \(2017\)](#).